Computers and Geotechnics 187 (2025) 107462

Contents lists available at ScienceDirect

Computers and Geotechnics

journal homepage: www.elsevier.com/locate/compgeo

Research paper

Accounting for cyclic and fabric effects in an enhanced hypoplastic model for sand

L. Mugele [a,*], H.H. Stutz [a], Z.X. Yang [b]

[a] Institute of Soil Mechanics and Rock Mechanics (IBF), Karlsruhe Institute of Technology (KIT), Engler-Bunte-Ring 14, Karlsruhe, 76131, Baden-Württemberg, Germany

[b] Department of Civil Engineering, Zhejiang University, Hangzhou, 310058, China

ARTICLE INFO

Keywords:
Hypoplasticity
Generalized intergranular strain
Asymptotic state boundary surface
Anisotropic critical state theory
Fabric

ABSTRACT

An enhanced hypoplastic constitutive model accounting for anisotropic fabric effects in modeling the mechanical behavior of granular materials subjected to monotonic and cyclic loading is presented. Based on von Wolffersdorff's hypoplastic model (HP), the proposed formulation combines the recently published generalized intergranular strain (GIS) concept for the simulation of cyclic deformations and the anisotropic critical state theory (ACST) to account for the anisotropic fabric effects on the macroscopic stress–strain behavior. Using six state variables ($\boldsymbol{\sigma}$, e, $\boldsymbol{h}$, Ω, $\boldsymbol{F}$, H), the proposed enhanced hypoplastic model called HP+GIS+ACST can effectively reproduce the soil behavior under both monotonic and cyclic loading. The HP+GIS+ACST solves the overshooting problem of the asymptotic state boundary surface (ASBS) and reproduces soil liquefaction effects due to cyclic loading in loose as well as in dense samples. The model's performance is validated by simulating both monotonic and cyclic tests, with comparisons to experimental data from Karlsruhe fine sand (KFS) and Fraser River sand (FRS), as well as to two other hypoplastic models.

1. Introduction

The constitutive modeling of granular materials, such as sand, remains a complex task in soil mechanics. While advanced constitutive models nowadays can reproduce the overall highly non-linear behavior of soil — including contractancy, dilatancy, as well as density and pressure dependency (pyknotropy and barotropy) — two specific challenges in modeling the macroscopic stress–strain behavior of soils are still widely discussed: (1) small-strain effects, particularly under cyclic loading conditions, and (2) anisotropic fabric effects, which account for the influence of the soil's microscopic structure on its macroscopic stress–strain behavior. In general, these challenges are relevant across various constitutive modeling frameworks, including bounding surface, elastoplastic, and hypoplastic constitutive models.

Hypoplasticity is a promising framework for reproducing the mechanical behavior of soil. In such models, the norm of the strain rate $\|\dot{\epsilon}\|$ replaces the plastic strain rate $\dot{\epsilon}^{\mathrm{pl}}$ used in elastoplastic models to simulate irreversible deformations. Hypoplastic formulations do not require the decomposition of the total strain rate into an elastic and a plastic part without invoking a yield surface or plastic potential. Instead, hypoplastic formulations rely on a single tensorial equation that relates the effective stress rate $\dot{\boldsymbol{\sigma}}$ to the strain rate $\dot{\boldsymbol{\epsilon}}$. A detailed overview of hypoplastic models is provided by Mašín (2019).

Early versions of hypoplastic constitutive models utilized only the effective stress $\boldsymbol{\sigma}$ as a state variable (Kolymbas, 1988, 1991a,b; Wu and Bauer, 1994). The critical state concept (Roscoe et al., 1958; Schofield and Wroth, 1968) was later integrated by incorporating the void ratio e as an additional state variable (Bauer, 1996; Gudehus, 1996). The nowadays widely-used version proposed by von Wolffersdorff (1996) (HP) includes the failure criterion according to Matsuoka and Nakai (1977). However, these two state variables ($\boldsymbol{\sigma}$, e) are insufficient to model loading direction reversals or cyclic deformations as the model's response for a loading direction reversal is too soft and accompanied by extensive irreversible deformations, known as ratcheting.

To address this issue, Niemunis and Herle (1997) introduced the intergranular strain (IS) concept. They added a tensorial state variable, called intergranular strain $\boldsymbol{h}$, memorizing the most recent deformation history. The resulting coupled HP+IS model prevents the ratcheting under specific stress or strain amplitudes and is nowadays widely used for geotechnical analyses involving both monotonic and cyclic deformations (Chrisopoulos and Vogelsang, 2019; Norlyk et al., 2020; Staubach et al., 2021).

Despite its success, the HP+IS still reveals several shortcomings (Duque et al., 2022; Mugele et al., 2024a) and various improvements have therefore be proposed in the literature (Wegener and Herle, 2014;

* Corresponding author.
E-mail addresses: luis.mugele@kit.edu (L. Mugele), hans.stutz@kit.edu (H.H. Stutz), zxyang@zju.edu.cn (Z.X. Yang).

https://doi.org/10.1016/j.compgeo.2025.107462
Received 11 November 2024; Received in revised form 25 May 2025; Accepted 27 June 2025
Available online 11 July 2025

Fuentes and Triantafyllidis, 2015; Poblete et al., 2016; Bode et al., 2020; Duque et al., 2020). The recently published generalized intergranular strain (GIS) concept (Mugele et al., 2024b) coupled with the HP (HP+GIS) overcomes the overshooting of the so-called asymptotic state boundary surface (ASBS) and thus prevents an overestimation of strength due to small unloading and reloading cycles. Furthermore, the GIS concept allows for the simulation of highly non-linear accumulation effects by using an additional scalar state variable called cyclic preloading Ω.

Additionally, it is well known that the current anisotropic fabric (anisotropic microstructure) of a soil sample significantly influences its overall macroscopic behavior (Oda, 1972; Miura and Toki, 1984; Yang et al., 2008; Wichtmann, 2016). This aspect is not considered in the hypoplastic models mentioned above. However, a large number of non-hypoplastic models considering an evolving anisotropic fabric can be found in the literature. These include for example the Sanisand models (Dafalias and Manzari, 2004; Petalas et al., 2019, 2020), the PM4Sand model (Boulanger and Ziotopoulou, 2022) and other constitutive formulations (Andrianopoulos et al., 2010; Gao and Zhao, 2015; Yang et al., 2018; Wang et al., 2021).

To account for anisotropic fabric effects in hypoplastic models, Yang et al. (2020) and Liao and Yang (2021) implemented the anisotropic critical state theory (ACST) proposed by Li and Dafalias (2012) in the hypoplastic framework. By incorporating a second-order deviatoric fabric tensor $\boldsymbol{F}$ and a scalar-valued state variable memorizing the dilation history H, the extended model by Liao and Yang (2021), further called HP+IS+ACST, can reproduce the effect of bedding plane, shear modes, anisotropic failure surfaces, and the liquefaction phenomena under cyclic loading in both loose and dense soils. It is worth noting that in recent years, hypoplastic constitutive models have also been proposed that include an evolving fabric tensor, but without incorporating the ACST framework (Niemunis and Grandas Tavera, 2019; Fuentes et al., 2020; Liao et al., 2022; Tafili et al., 2024a).

In this work, an enhanced hypoplastic model is proposed, combining the two mentioned enhancements of the HP+IS formulation: the GIS approach and the ACST framework. The new model is referred to as HP+GIS+ACST and addresses some of the major issues of each former hypoplastic formulation (HP+IS, HP+GIS, and HP+IS+ACST). More specifically, it resolves the issues related to overshooting of the ASBS, linear accumulation, lack of fabric effects, and non-achievement of soil liquefaction due to cyclic loading of dense samples. The feasibility of the novel model is demonstrated using simulations of element tests, which are compared with experimental data of Karlsruhe fine sand (KFS) and Fraser River sand (FRS). Comparative simulations using HP+GIS and HP+IS+ACST demonstrate the major merits of HP+GIS+ACST.

The novel HP+GIS+ACST model is based on the extended generalized hypoplasticity proposed by Mugele et al. (2024b), which is discussed in Section 2. Section 3 describes the GIS concept, and Section 4 provides an overview of the ACST framework and introduces the novel HP+GIS+ACST formulation. A theoretical discussion of the coupling of the ACST with a constitutive model is given in Section 5. Simulations of element tests are presented and compared with experimental data in Section 6. The results are summarized in Section 7. Notation and abbreviations used throughout this paper are presented in Appendix B.

2. Extended generalized hypoplasticity

Early rate-independent and incrementally non-linear hypoplastic models relied solely on the effective Cauchy stress $\boldsymbol{\sigma}$ as a state variable. These models were initially developed through heuristic methods and are based on the general representation theorem for isotropic tensor functions of two symmetric tensorial arguments ($\boldsymbol{\sigma}$ and $\dot{\boldsymbol{\varepsilon}}$) (Kolymbas, 1988, 1991a,b). Later, the hypoplastic equation

$$\dot{\boldsymbol{\sigma}} = \mathsf{L} : \dot{\boldsymbol{\varepsilon}} + \boldsymbol{N}\|\dot{\boldsymbol{\varepsilon}}\| \tag{1}$$

with the fourth-order tensor L (linear term) and the second-order tensor $\boldsymbol{N}$ (non-linear term), which are both functions of the effective Cauchy stress only, have been established (Wu, 1992; Wu and Bauer, 1994). Using the void ratio e as an additional state variable and introducing the barotropy and pyknotropy factors (f_s and f_d), critical state conform hypoplastic models have been developed (Bauer, 1996; Gudehus, 1996). They can be generally expressed as:

$$\dot{\boldsymbol{\sigma}} = f_s \mathsf{L} : \dot{\boldsymbol{\varepsilon}} + f_s f_d \boldsymbol{N}\|\dot{\boldsymbol{\varepsilon}}\| \ . \tag{2}$$

Mainly driven by the work of Mašín and Herle (2005) and Mašín (2012, 2013, 2019), rate-independent hypoplastic models can also be written using the so-called asymptotic state boundary surface (ASBS). An asymptotic state (also known as an attractor or a swept-out-memory state) is a state reached after sufficient long monotonic proportional deformation (Mašín and Herle, 2005, 2006; Gudehus and Mašín, 2009; Gudehus, 2011; Mašín, 2019). The ASBS summarizes all asymptotic states including the well-known critical states, which are achieved by proportional volume-constant strain paths. If an ASBS is explicitly defined, such as in some clay models (Mašín, 2012, 2013), the fourth-order tensor A representing the stiffness for a virgin loading, the pyknotropy factor in the asymptotic state f_d^A, and the asymptotic strain rate direction $\boldsymbol{d}$ are specified. A hypoplastic constitutive model with explicitly defined ASBS can be directly formulated:

$$\dot{\boldsymbol{\sigma}} = f_s \mathsf{L} : \dot{\boldsymbol{\varepsilon}} - \frac{f_d}{f_d^A} \mathsf{A} : \boldsymbol{d}\ \|\dot{\boldsymbol{\varepsilon}}\| \ . \tag{3}$$

Using

$$\boldsymbol{N} = -\frac{\mathsf{A} : \boldsymbol{d}}{f_s f_d^A} \ , \tag{4}$$

Eq. (3) can be rewritten:

$$\dot{\boldsymbol{\sigma}} = f_s \mathsf{L} : \dot{\boldsymbol{\varepsilon}} + f_s \frac{f_d}{f_d^A} f_d^A \boldsymbol{N}\|\dot{\boldsymbol{\varepsilon}}\| \ . \tag{5}$$

In contrast to Eq. (3), Eq. (5) can be applied to any hypoplastic model written in the form of Eq. (2), where the pyknotropy factor in the asymptotic state f_d^A is explicitly defined or can be derived without the knowledge about A and $\boldsymbol{d}$.

Every hypoplastic constitutive model, which can be written in terms of Eqs. (1)–(3) or Eq. (5), can be mathematically equivalent reformulated using the recently proposed extended generalized hypoplasticity (Mugele et al., 2024b):

$$\dot{\boldsymbol{\sigma}} = \mathsf{E} : (\dot{\boldsymbol{\varepsilon}} - \boldsymbol{m}\ C\ S\ \|\dot{\boldsymbol{\varepsilon}}\|) \ . \tag{6}$$

Eq. (6) includes the elastic stiffness E, the hypoplastic equivalent flow rule $\boldsymbol{m}$, and the so-called state mobilization S indicating if a current state lies on the ASBS ($S = 1$) or not. A model formulated in terms of Eq. (5) can be reformulated into Eq. (6) using

$$\mathsf{E} = \mathsf{L} f_s \ , \tag{7}$$

$$\boldsymbol{m} = -[\mathsf{L}^{-1\vec{}} : \boldsymbol{N}] \ , \tag{8}$$

$$C = \|\mathsf{L}^{-1} : \boldsymbol{N}\| f_d^{A*} \ , \tag{9}$$

$$S = f_d / f_d^{A*} \ . \tag{10}$$

If f_d^A is explicitly defined, then $f_d^{A*} = f_d^A$ applies. If f_d^A is not known per definition, a similar quantity f_d^{A*} can be defined. If neither f_d^A nor f_d^{A*} can be derived, but Eq. (2) holds, $S = Y$ and $C = 1$ can be set using the so-called degree of non-linearity Y (Niemunis, 2003). The scalar parameter C is introduced for generalization.

Nowadays, the hypoplasticity after von Wolffersdorff (1996) (HP) is widely used for modeling granular soil subjected to monotonic loading. This model involves two state variables: the effective Cauchy stress $\boldsymbol{\sigma}$ and the void ratio e (isotropic measurement of the microstructure of a

soil sample) and considers the failure criterion by Matsuoka and Nakai (1977). The equations of the original HP can be found in Appendix B. In the HP, the ASBS is not explicitly defined. However, as shown by Mašín and Herle (2006), the HP implicitly contains the ASBS and the latter can be found using an iterative procedure. Following the approach detailed in Mašín and Herle (2006) and Mugele et al. (2024b), and assuming that a given state lies on the ASBS, one can calculate f_d^{A*} using

$$\boldsymbol{B} = \mathsf{L}^{-1} : \boldsymbol{N} \,, \tag{11}$$

$$\boldsymbol{C} = 1/f_s(\mathsf{L}^{-1} : \vec{\boldsymbol{\sigma}}) \,, \tag{12}$$

$$G = \frac{n}{h_s} \operatorname{tr} \vec{\boldsymbol{\sigma}} \left(\frac{3p}{h_s}\right)^{(n-1)} \,, \tag{13}$$

with

$$f_d^{A*} = \sqrt{\left[\|\boldsymbol{B}\|^2 + \left(\frac{\|\boldsymbol{C}\|\left(\frac{1+e}{e}\right)\operatorname{tr}\boldsymbol{B}}{G - \left(\frac{1+e}{e}\right)\operatorname{tr}\boldsymbol{C}}\right)^2 + \frac{2(\boldsymbol{B} : \boldsymbol{C})\operatorname{tr}\boldsymbol{B}\left(\frac{1+e}{e}\right)}{G - \left(\frac{1+e}{e}\right)\operatorname{tr}\boldsymbol{C}}\right]^{-1}} \,. \tag{14}$$

According to Eq. (10), the comparison of f_d^{A*} with the current pyknotropy factor

$$f_d = \left(\frac{e - e_d}{e_c - e_d}\right)^{\alpha} \tag{15}$$

can be further used to define the state mobilization S. For $S = 1$, the current state lies on the ASBS. For $S < 1$, the state is located inside the ASBS, while for $S > 1$, the current state lies outside the ASBS. Note that in hypoplastic models $S > 1$ is generally possible, as the ASBS does not correspond to the state boundary surface (Mašín and Herle, 2005). The reformulated HP model using Eq. (6) is mathematically equivalent to the original model, however includes additional information regarding the ASBS.

3. Generalized intergranular strain concept

The previously considered HP is well suited for the simulation of monotonic deformations of granular material but it fails in the simulation of loading direction reversals and cyclic deformation due to the so-called ratcheting, i.e. a too soft response as a result of a loading direction reversal. To overcome this issue, Niemunis and Herle (1997) introduced the intergranular strain (IS) concept. For details, it is referred to the literature (Niemunis and Herle, 1997; Niemunis, 2003; Mašín, 2019). The original IS concept coupled with a base constitutive model such as HP can be used for the investigation of many practical problems including cyclic deformation but, in detail, still exhibits a couple of shortcomings (Duque et al., 2022).

To overcome two major issues of the original IS approach namely the so-called overshooting and linear accumulation, Mugele et al. (2024b) proposed the generalized intergranular strain (GIS) concept. The GIS approach is based on a reinterpretation of the original IS concept and combines it with several IS improvements from the literature (Wegener and Herle, 2014; Poblete et al., 2016; Duque et al., 2020). The state variable intergranular strain $\boldsymbol{h}$ memorizes the most recent deformation history and the evolution equation reads

$$\dot{\boldsymbol{h}} = \begin{cases} (\mathrm{I} - \vec{\boldsymbol{h}}\vec{\boldsymbol{h}}\rho^{\beta_R}) : \dot{\boldsymbol{\varepsilon}} & \text{if } \vec{\boldsymbol{h}} : \dot{\boldsymbol{\varepsilon}} > 0 \\ \dot{\boldsymbol{\varepsilon}} & \text{if } \vec{\boldsymbol{h}} : \dot{\boldsymbol{\varepsilon}} \le 0 \end{cases} \,, \tag{16}$$

whereby β_R is a constitutive parameter. The direction of the intergranular strain $\vec{\boldsymbol{h}}$ is defined as

$$\vec{\boldsymbol{h}} = \begin{cases} \frac{\boldsymbol{h}}{\|\boldsymbol{h}\|} & \text{if } \boldsymbol{h} \neq \boldsymbol{0} \\ \boldsymbol{0} & \text{if } \boldsymbol{h} = \boldsymbol{0} \end{cases} \tag{17}$$

and for the degree of mobilization of the intergranular strain applies

$$\rho = \frac{\|\boldsymbol{h}\|}{R} \,, \tag{18}$$

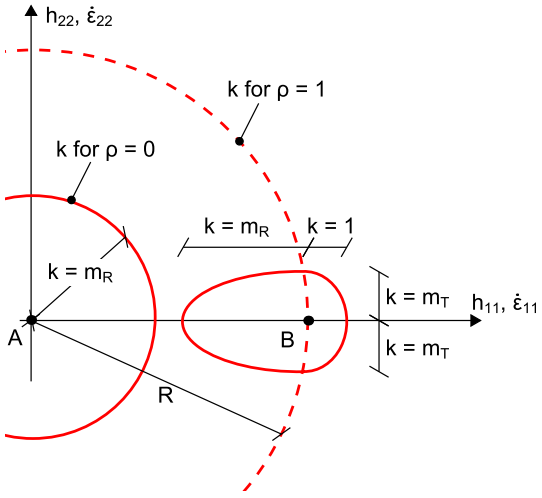

Fig. 1. Scalar factor k in the GIS concept as a function of the parameters m_R and m_T for $\rho = 0$ and $\rho = 1$ in the two-dimensional case depending on the applied strain rate $\dot{\varepsilon}_{11}$ or $\dot{\varepsilon}_{22}$.
Source: Mugele et al. (2024b).

with $0 \le \rho \le 1$, whereby the parameter R quantifies the elastic range. A sufficiently large monotonic deformation leads asymptotically to $\dot{\boldsymbol{h}} = 0$ with $\rho = 1$. A scalar factor k is defined in the GIS concept as:

$$k = [\rho^{\chi_R} m_T + (1 - \rho^{\chi_R}) m_R] + \begin{cases} \rho^{\chi_R}(1 - m_T)\vec{\boldsymbol{h}} : \vec{\boldsymbol{\varepsilon}} & \text{if } \vec{\boldsymbol{h}} : \dot{\boldsymbol{\varepsilon}} > 0 \\ -\rho^{\chi_R}(m_R - m_T)\vec{\boldsymbol{h}} : \vec{\boldsymbol{\varepsilon}} & \text{if } \vec{\boldsymbol{h}} : \dot{\boldsymbol{\varepsilon}} \le 0. \end{cases} \tag{19}$$

In fact, Eq. (19) provides an interpolation for the factor k, which depends on the current intergranular strain $\boldsymbol{h}$, its mobilization $\rho = \frac{\|\boldsymbol{h}\|}{R}$, and the applied strain rate direction $\vec{\boldsymbol{\varepsilon}}$. The parameters m_R, m_T and χ_R govern the interpolation between the minimum value $k = 1$ and the maximum value $k = m_R$. $k = 1$ and $\rho = 1$ are reached asymptotically due to a monotonic strain path. $k = m_R$ occurs due to a 180° loading direction reversal at $\rho = 1$ and $k = m_T$ results for a 90° loading direction reversal at $\rho = 1$. $k = m_R$ holds at $\rho = 0$, irrespective of the applied strain rate. Eq. (19) and the discussed special cases are visualized in Fig. 1 in two dimensions.

The factor k can be used further to achieve an (I) increase of the stiffness and a (II) reduction of irreversible deformations in the base constitutive model formulated using the extended generalized hypoplasticity (Eq. (6)):

$$\dot{\boldsymbol{\sigma}} = k\, \mathsf{E} : \left(\dot{\boldsymbol{\varepsilon}} - \boldsymbol{m}\, C\, S^{(k^{\gamma})}\, \|\dot{\boldsymbol{\varepsilon}}\|\right) \,, \tag{20}$$

The exponent γ is calculated with the function $\chi(\Omega)$ using the scalar cyclic preloading state variable Ω and the material parameter γ_χ:

$$\gamma = \gamma_\chi \chi \,. \tag{21}$$

Following an approach first proposed by Poblete et al. (2016) and adapted by Duque et al. (2020) to the original IS concept, the function

$$\chi = \chi_0 + \Omega\left(\chi_{\max} - \chi_0\right) \tag{22}$$

is defined using the parameters χ_0 and $\chi_{\max}$. The state variable Ω approaches unity ($\Omega \to 1$) for cyclic loading with small amplitudes when the intergranular strain is not mobilized ($\rho \approx 0$). It vanishes to zero during sufficiently long monotonic deformation or cyclic loading with large strain amplitudes with $\rho \approx 1$. The evolution equation of the cyclic preloading variable reads:

$$\dot{\Omega} = C_\Omega\left(1 - \rho^{\gamma_\Omega} - \Omega\right)\|\dot{\boldsymbol{\varepsilon}}\| \,. \tag{23}$$

$0.0 \leq \Omega \leq 1.0$ holds and details can be found in Poblete et al. (2016) and Duque et al. (2020).

A comparison between Eq. (6) and Eq. (20) shows that the effect of a loading direction reversal ($k > 1$) on the reduction of irreversible deformations at a state lying on the ASBS vanishes due to the condition $S = 1 = S^k$, which significantly reduces the overshooting of the ASBS.

4. Hypoplasticity coupled with the anisotropic critical state theory

The microstructure of soil can be described using statistical characteristics of the spatial distribution of soil particles and the voids between them (Li and Li, 2009; Wiebicke et al., 2021). The scalar void ratio e, which is a widely accepted state variable in advanced constitutive models for soil, corresponds to the isotropic part of the microstructure. To characterize the anisotropic part of the microstructure, a second-order deviatoric fabric tensor $\boldsymbol{F}$ can be defined (Li and Li, 2009; Yang and Wu, 2017). Based on such a tensor, Li and Dafalias (2012) proposed the so-called anisotropic critical state theory (ACST). This theory extends the well-known critical state theory (Roscoe et al., 1958; Schofield and Wroth, 1968) by the effect of an anisotropic fabric. For the second-order deviatoric anisotropic fabric tensor, further just called fabric, applies:

$$\boldsymbol{F} = F\boldsymbol{n}_F, \quad \text{with} \quad F = \sqrt{\boldsymbol{F} : \boldsymbol{F}} = \|\boldsymbol{F}\| , \tag{24}$$

and

$$\boldsymbol{n}_F : \boldsymbol{n}_F = 1, \quad \operatorname{tr} \boldsymbol{F} = 0, \quad \operatorname{tr} \boldsymbol{n}_F = 0 , \tag{25}$$

where $F = \|\boldsymbol{F}\|$ is the norm and $\boldsymbol{n}_F = \vec{\boldsymbol{F}}$ is the unit direction of the fabric tensor $\boldsymbol{F}$. Due to a proportional monotonic deformation with $\dot{\boldsymbol{\varepsilon}} \neq \boldsymbol{0}$, the fabric tends towards an asymptotic value $\boldsymbol{F}^{\text{asy}}$. This asymptotic fabric depends on the applied deformation path. In the critical state, which is reached upon a volume constant proportional strain path, the norm of the fabric tends to its critical value. It is reasonable to normalize the fabric tensor $\boldsymbol{F}$ with its critical state value (Yang et al., 2020). Doing so, $\|\boldsymbol{F}^{\text{asy,c}}\| = F^{\text{asy,c}} = 1$ applies in the critical state. The direction of the fabric tensor aligns in any asymptotic state for $\dot{\boldsymbol{\varepsilon}} \neq \boldsymbol{0}$ with the loading direction represented by the unit-norm deviatoric tensor $\boldsymbol{n}$.

Li and Dafalias (2012) introduced further a fabric anisotropy variable (FAV) A to quantify the relation between the current anisotropic fabric $\boldsymbol{F}$ and its loading direction $\boldsymbol{n}$:

$$A = \boldsymbol{F} : \boldsymbol{n} = F \underbrace{\boldsymbol{n}_F : \boldsymbol{n}}_{N} = FN . \tag{26}$$

Where, $N = \boldsymbol{n}_F : \boldsymbol{n}$ represents the relative orientation between the fabric tensor $\boldsymbol{F}$ and its loading direction $\boldsymbol{n}$. It is evident that $A^{\text{asy,c}} = 1$ applies in the critical state. The Been and Jefferies (1985) parameter

$$\psi = e - e_c(p) . \tag{27}$$

measures the distance between the current void ratio e and the critical void ratio e_c under the same mean effective pressure p and can be used to quantify the current state of the soil. For states lying below the critical state line (CSL) $e_c(p)$ in the $e - p$ plane (dense soil), the state parameter is negative ($\psi < 0$). Loose soils are characterized by a positive state parameter ($\psi > 0$) and in the critical state, $\psi = 0$ applies. To include the effect of fabric anisotropy within the ACST framework, a dilatancy state line (DSL) $e_{\text{dil}}(p, A)$ is defined in the $e - p$ plane

$$e_{\text{dil}} = e_c(p) + \underbrace{e_A(A - 1)}_{\psi_A} , \tag{28}$$

where $\psi_A = e_A(A-1)$ measures the distance between the fixed CSL and the variable, from the FAV A dependent, DSL at the same pressure p. At the critical state ($A = 1$), the DSL and the CSL correspond to each other ($\psi_A = 0$), maintaining the uniqueness of the CSL (Li and Dafalias, 2012). The concept is illustrated in Fig. 2.

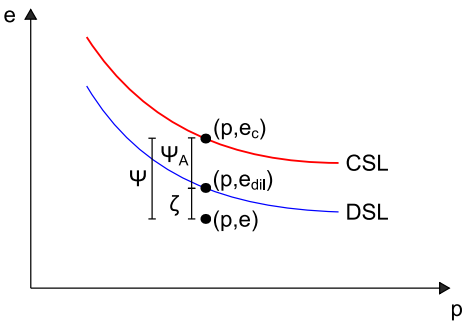

Fig. 2. Illustration of the parameters in the anisotropic critical state theory (ACST).
Source: Modified from Li and Dafalias (2012).

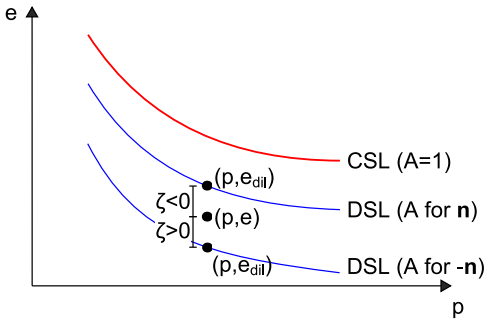

Fig. 3. Effect of a 180° reversal in the loading direction from $\boldsymbol{n}$ to $-\boldsymbol{n}$ on the dilatancy state line (DSL).
Source: Modified from Li and Dafalias (2012).

The ACST accounts implicitly for the effect of loading direction reversals on the dilatancy, as shown in Fig. 3. For a given state (e, p, $\boldsymbol{F}$) with a loading direction $\boldsymbol{n}$ and an anisotropic fabric $\boldsymbol{F}$, $A_1 = \boldsymbol{F} : \boldsymbol{n}$ applies. Lets assume $A_1 > 0$. When the loading direction changes due to an 180° reversal from $\boldsymbol{n}$ to $-\boldsymbol{n}$, the FAV becomes $A_2 = -\boldsymbol{F} : \boldsymbol{n} = -A_1$. The new DSL_2 shifts below the former DSL_1. The reduced e_{dil} enhances the contractive soil behavior upon reversal loading.

The briefly described ACST represents a standalone theory. However, this theory has already been included in some advanced constitutive models such as elastoplastic formulations (Yang et al., 2018), bounding surface models (Gao and Zhao, 2015; Petalas et al., 2019, 2020) and hypoplastic models (Yang et al., 2020; Liao and Yang, 2021), and will be further used to derive the novel HP+GIS+ACST.

Soil often exhibits a transverse isotropy in correspondence to the sedimentation axis. For an initially transversely isotropic soil with the bedding plane oriented along the $x_2 - x_3$ axes and the sedimentation direction aligned with the x_1 axis, the initial anisotropic fabric tensor $\boldsymbol{F}_0$ can be written

$$\boldsymbol{F}_0 = F_0\boldsymbol{n}_{F0} = F_0 \underbrace{\begin{bmatrix} -2/\sqrt{6} & 0 & 0 \\ 0 & 1/\sqrt{6} & 0 \\ 0 & 0 & 1/\sqrt{6} \end{bmatrix}}_{\boldsymbol{n}_{F0}} \tag{29}$$

with the initial fabric norm $\|\boldsymbol{F}_0\| = F_0$. The mechanical sign convention (compression negative) of the fabric tensor should be noted. Following Liao and Yang (2021), the loading direction of the fabric can be defined as the direction of the deviatoric strain rate:

$$\boldsymbol{n} = \frac{\dot{\boldsymbol{\varepsilon}}^*}{\|\dot{\boldsymbol{\varepsilon}}^*\|} \tag{30}$$

For an isotropic compression or extension ($\dot{\boldsymbol{\varepsilon}}^* = \mathbf{0}$) $\boldsymbol{n} = \mathbf{0}$ is defined. Assuming that the fabric evolves only due to a deviatoric strain rate and based on fabric evolution equations from the literature (Yang et al., 2020; Liao and Yang, 2021; Yang et al., 2018; Petalas et al., 2020), a slightly modified evolution equation for the anisotropic fabric is proposed. The fabric evolution equation reads

$$\dot{\boldsymbol{F}} = [\boldsymbol{n} - (1 + D)^{\alpha_D} \boldsymbol{F}]\ m\ \|\dot{\boldsymbol{\varepsilon}}^*\| \tag{31}$$

with the dilatancy

$$D = -\frac{\operatorname{tr} \dot{\boldsymbol{\varepsilon}}}{\|\dot{\boldsymbol{\varepsilon}}^*\|}\ . \tag{32}$$

If the volume of the soil increases, D is negative. The parameter m governs the rate of fabric evolution, while the proposed exponent α_D determines the extent to which the dilatancy D influences fabric evolution. Eq. (31) qualitatively captures two main characteristics of fabric evolution:

- The fabric tends toward an asymptotic value under proportional deformation as theoretically discussed in Yang et al. (2018). Under compressive proportional deformation (such as an oedometric or isotropic compression), the fabric tends to asymptotic values of $\|\boldsymbol{F}^{\text{asy}}\| < 1$, while under extensive proportional deformations, it tends toward $\|\boldsymbol{F}^{\text{asy}}\| > 1$. In the case of volume-constant proportional deformation with $\operatorname{tr} \dot{\boldsymbol{\varepsilon}} = 0$ for $\dot{\boldsymbol{\varepsilon}} \neq \mathbf{0}$, the dilatancy vanishes ($D = 0$). At a critical state, it follows that $\|\boldsymbol{F}^{\text{asy}}\| = 1$, which is confirmed by numerous discrete element simulations (Xie et al., 2017; Yang and Wu, 2017; Adesina et al., 2023; Wang et al., 2022, 2020). Furthermore, in the critical state, $A^{\text{asy,c}} = 1$ is attained, ensuring the uniqueness of the critical state as defined by Eq. (35).
- In dense samples subjected to monotonic shearing, the fabric exhibits a peak before reaching its critical state value. In contrast, loose samples do not show any peak in fabric (Xie et al., 2017; Yang and Wu, 2017; Adesina et al., 2023; Wang et al., 2020).

These features of Eq. (31) are demonstrated in Figs. 4 and 5 illustrating the fabric evolution for different parameters m and α_D. $F_0 = 0.5$ and a transverse isotropy is initialized. Fig. 4 shows the fabric evolution for different monotonic proportional axisymmetric strain paths, for which different asymptotic values of the fabric norm $\|\boldsymbol{F}^{\text{asy}}\| = F^{\text{asy}}$ are reached. It can also be seen that there is no evolution of the fabric in the case of a pure isotropic compression due to $\|\dot{\boldsymbol{\varepsilon}}^*\| = 0$. Fig. 5 shows the fabric evolution during monotonic drained triaxial tests with two different initial densities. While $D < 0$ applies for dense soil in the dilative phase leading to a peak in the fabric norm, $D > 0$ applies for loose soil during the entire deformation and the fabric does not reach a peak value. These results correspond qualitatively to discrete element simulations, which studied the evolution of the anisotropic microstructure in granular materials due to shear (Guo and Zhao, 2013; Yang and Wu, 2017; Adesina et al., 2023). Note that the dilatancy D in the drained triaxial tests is derived from the whole constitutive model and Eq. (31) can thus not be directly integrated.

The fabric anisotropy significantly influences the dilatancy of a soil sample. Experimental results indicate that sand specimens prepared using the dry deposition method is more dilative when the loading direction is more perpendicular to the bedding plane (Nemat-Nasser and Tobita, 1982; Yoshimine et al., 1998; Yang et al., 2008). The sample preparation technique also influences the initial dilatancy of a soil sample due to a different initialized fabric (Yang et al., 2008; Wichtmann and Triantafyllidis, 2016b).

Following the approach after Yang et al. (2020), the FAV A is included in the HP by modifying the upper and lower bounds of the void ratio $e_i(p)$ and $e_d(p)$ as well as the CSL in the $e - p$ plane $e_c(p)$:

$$e_i = e_{i0} \exp\left[-\left(\frac{-\operatorname{tr} \boldsymbol{\sigma}}{h_s}\right)^n\right] + e_A(A - 1)\ , \tag{33}$$

$$e_d = e_{d0} \exp\left[-\left(\frac{-\operatorname{tr} \boldsymbol{\sigma}}{h_s}\right)^n\right] + e_A(A - 1)\ , \tag{34}$$

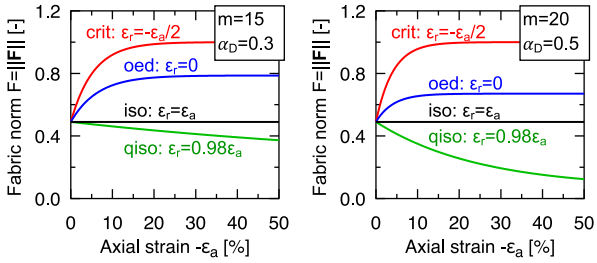

Fig. 4. Evolution of the norm of the fabric $\|\boldsymbol{F}\| = F$ for different parameters m and α_D due to different axisymmetric proportional strain paths.

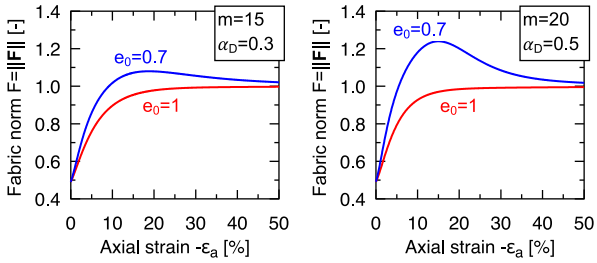

Fig. 5. Evolution of the norm of the fabric $\|\boldsymbol{F}\| = F$ for different parameters m and α_D due to triaxial compression tests for different initial densities with $p_0 = 200$ kPa, $\boldsymbol{h}_0 = -0.77\ R/\sqrt{3}\boldsymbol{\delta}$, $\Omega_0 = 0$, $F_0 = 0.5$ and $H_0 = 0$ for parameters of KFS.

$$e_c = e_{c0} \exp\left[-\left(\frac{-\operatorname{tr} \sigma}{h_s}\right)^n\right] + e_A(A - 1)\ , \tag{35}$$

with

$$e_A = e_{A0} \exp\left[-\left(\frac{-\operatorname{tr} \boldsymbol{\sigma}}{h_s}\right)^n\right]\ /\ k\ . \tag{36}$$

Eq. (36) ensures that the shift of the limit void ratios tends to zero for high mean effective pressures. Numerical element test simulations revealed that the incorporation of the factor k in Eq. (36) from the GIS concept provided improved results. In particular, more realistic accumulation effects could be simulated in cyclic tests with small strain amplitudes. The value of e_{A0} could be set as a constant (Yang et al., 2020). However, To improve simulations for cyclic mobility of dense sand, e_{A0} should increase due to dilative deformations, which occur beyond the phase transformation line (Liao and Yang, 2021). If the stress state intersects the phase transformation line can be approximated using (Fuentes et al., 2020)

$$F_d = \frac{q/p}{M_c F^{\text{hyp}} f_d} - 1\ , \tag{37}$$

where $p = -\operatorname{tr} \boldsymbol{\sigma}/3$ represent the mean effective pressure, $q = \sqrt{3/2}\|\boldsymbol{\sigma}^*\|$ is the deviatoric stress (Roscoe invariants) and f_d is the pyknotropy factor. F^{hyp} characterizes the shape of the critical state surface by Matsuoka and Nakai (1977) including the effect of fabric anisotropy according to Eq. (40) and $M_c = (6 \sin \varphi_c)/(3 - \sin \varphi_c)$ denotes the critical stress ratio for triaxial compression. Note that the pyknotropy factor f_d in Eq. (37) is calculated considering the influence of the FAV A on the limit void ratios according to Eqs. (33)–(35).

The non-constant value of e_{A0} can be expressed by

$$e_{A0} = k_1 + k_2 \frac{H}{1 + H} \tag{38}$$

using an additional scalar state variable H first proposed by Liao and Yang (2021) and further called dilation history. The dilation history H is an empirical quantity memorizing previous deformations associated with dilatancy. The larger H, the larger becomes e_{A0}. The parameters k_1 and k_2 define the maximum and minimum values of

e_{A0}. A larger value of e_{A0} enhances the fabric effect on the overall mechanical behavior, see Eqs. (33)–(36). Using the dilation history H, the constitutive model can account for the fact that dilative behavior causes significant rearrangement of particles. This rearrangement leads to increased contractive behavior upon loading reversal, as discussed for example in Dafalias and Manzari (2004) and Nemat-Nasser and Tobita (1982), and is incorporated in various constitutive models from different frameworks (Dafalias and Manzari, 2004; Andrianopoulos et al., 2010; Niemunis et al., 2016; Fuentes et al., 2020; Boulanger and Ziotopoulou, 2022; Tafili et al., 2024a). The evolution equation of the dilation history H reads

$$\dot{H} = \mu_0 \langle F_d \rangle \|\dot{\boldsymbol{\varepsilon}}\| - H c_r \langle -F_d / |F_d| \rangle |\operatorname{tr} \dot{\boldsymbol{\varepsilon}}| \,. \tag{39}$$

The parameter μ_0 controls the increase of H, which occurs only for positive values of F_d (Macauley brackets $\langle F_d \rangle$ in Eq. (39)) and thus only in the dilative deformation phase. For continuous dilation, the dilation history increases from its initial value H_0 to $H = \infty$. For $H_0 = 0$, according to Eq. (38), e_{A0} increases from k_1 to $(k_1 + k_2)$ with increasing H, intensifying the fabric effect on dilatancy.

Based on the work of Barrero et al. (2020) and the theory of the so-called semifluidized state, the reducing part of Eq. (39) is introduced. This part ensures a decrease of the dilation history H due to a compressive deformation (negative value of F_d and $|\operatorname{tr} \dot{\boldsymbol{\varepsilon}}| > 0$). The decrease can be controlled by the parameter c_r and ensures the erasure of the dilation history H, for example, due to a reconsolidation after a cyclic mobility phase. However, the parameter c_r has not been calibrated and for all simulations $c_r = 1$ has been chosen within this work.

In addition to the dilatancy, the strength of soil can be significantly affected by the fabric anisotropy (Kirkgard and Lade, 1993; Yang et al., 2020). To account for the influence of fabric anisotropy on soil strength, the FAV A can be used to modify the Matsuoka and Nakai (1977) criterion as proposed by (Liao and Yang, 2021)

$$F^{\text{hyp}} = F_0^{\text{hyp}} \exp[\lambda(A - 1)] \tag{40}$$

where λ is a positive model parameter, and F_0^{hyp} represents the original hypoplastic expression according to Eq. (B.6). The FAV A decreases as the angle between the loading direction and the fabric increases. Consequently, F^{hyp} also decreases, which models the anisotropic strength.

5. Theoretical aspects of the novel HP+GIS+ACST

The novel hypoplastic constitutive model HP+GIS+ACST is now fully defined, combining the hypoplasticity after von Wolffersdorff (1996) (HP), the generalized intergranular strain (GIS) concept (Mugele et al., 2024b) and the anisotropic critical state theory (ACST) (Li and Dafalias, 2012). However, some theoretical aspects of the HP+GIS+ACST should be discussed. Note that the following discussion is not limited to HP+GIS+ACST. It should be expected that these points will generally apply to all constitute models coupled with the ACST, especially if an advanced evolution equation for the anisotropic fabric is included.

(1) The evolution equation of the anisotropic fabric (Eq. (31)) results in different asymptotic values of the FAV A^{asy} for different proportional strain paths, which is consistent with the literature (Yang et al., 2018). It follows that the coupling of the ACST with the HP leads to a different shape of the ASBS compared to the one predicted by the original HP model. Only the critical states remain unchanged. Additionally, the shape and the size of the ASBS depend on e_{A0}.

(2) If $\|\dot{\boldsymbol{\varepsilon}}^*\| = 0$ (isotropic compression) applies for a proportional strain path with $\dot{\boldsymbol{\varepsilon}} \neq \mathbf{0}$, $\dot{\boldsymbol{F}} = \mathbf{0}$ and therefore $\boldsymbol{F}^{\text{asy,iso}} = \boldsymbol{F}_0$ results from Eq. (31). In contrast, due to a proportional quasi-isotropic strain path with $\|\dot{\boldsymbol{\varepsilon}}^*\| > 0$ but $\|\dot{\boldsymbol{\varepsilon}}^*\| \ll |\operatorname{tr} \dot{\boldsymbol{\varepsilon}}|$, $\boldsymbol{F}$ tends to zero leading to $\|\boldsymbol{F}^{\text{asy,qiso}}\| = F^{\text{asy,qiso}} = 0$ and $A^{\text{asy,qiso}} = 0$. However, $\boldsymbol{n} = \mathbf{0}$ is defined for an isotropic compression resulting in $A^{\text{asy,iso}} = 0$.

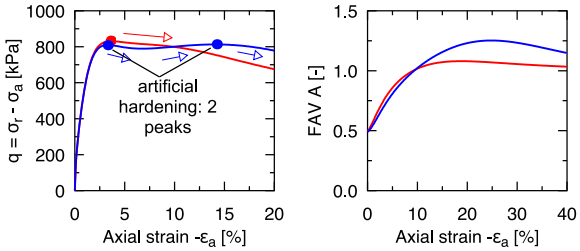

Fig. 6. Artificial hardening in a drained monotonic triaxial test on a dense sample: deviatoric stress $q = \sigma_r - \sigma_a$ and FAV A as a function of the axial strain ε_a for a suitable parameter set (KFS from Table 1) and an unsuitable parameter set ($m = 10$ and $\alpha_D = 0.8$) with $p_0 = 200$ kPa, $e_0 = 0.7$, $\boldsymbol{h}_0 = -0.77\, \boldsymbol{R}/\sqrt{3}\boldsymbol{\delta}$, $\boldsymbol{\Omega}_0 = 0$, $F_0 = 0.5$ and $H_0 = 0$.

(3) For an asymptotic state reached by a monotonic compressive proportional deformation with $\dot{\boldsymbol{\varepsilon}} \neq \mathbf{0}$ and for an isotropic compression, $\dot{e}_{A0} = 0$ and $\dot{A} = 0$ hold. The compression law of HP+ACST+GIS, Eqs. (33)–(36), can then be written in rate form as

$$\dot{e} = -e \left(\frac{3p}{h_s} \right)^{n-1} \frac{3n}{h_s} \dot{p} \,, \tag{41}$$

which coincides with the rate form of the original compression law according to Bauer (1996) given in Eq. (B.11). The barotropy factor f_s of the HP, as given in Eq. (B.9), still satisfies the consistency condition for isotropic compression even with the modified compression law (Niemunis et al., 2000). Furthermore, the expression for f_d^{A*}, Eq. (14), remains unchanged (Mašín and Herle, 2006).

(4) An artificial hardening can occur in dense samples after reaching the first peak stress if a poorly calibrated parameter set is used. The issue is demonstrated for a monotonic drained triaxial test in Fig. 6.

(5) In fact, the basic idea of the ACST is quite simple: the anisotropic fabric reveals the soil to behave like a looser one without an anisotropic fabric before reaching the critical state. However, base constitutive models are often used which do not adequately reproduce the dilation of dense soils (such as the HP). The combination of such base models with the ACST tends to exacerbate the problem of underestimating the dilation of dense soils.

(6) A curiosity should be noted regarding the simulation of the influence of the sample preparation method within the ACST: a more isotropic microstructure in moist tamped (MT) samples than in air pluviated (AP) samples is often documented in the literature (Miura and Toki, 1982; Yang et al., 2008; Wichtmann, 2016). In the ACST framework, this would require $|F_0^{\text{MT}}| < |F_0^{\text{AP}}|$ for the initialization of the fabric tensor. According to Eqs. (26) and (29), such initialization would result in $A_0^{\text{MT}} < A_0^{\text{AP}}$ for a triaxial compression, causing MT samples to show a more pronounced contractive behavior than AP samples. This would contradict experimental results. To reproduce the latter qualitatively, $|F_0^{\text{MT}}| > |F_0^{\text{AP}}|$ must be initialized. This initialization may be somehow attributed to the layering of the sample introduced by the MT sample preparation technique on a larger scale compared to the relatively isotropic grain contact distribution on the microstructure.

The points mentioned may not be crucial in practice, but a proper parameter calibration procedure is required.

6. Model performance and comparison

Simulations using the novel HP+GIS+ACST model are compared in the following against experimental data of Karlsruhe fine sand (KFS),

an extensively tested material from the literature (Wichtmann and Triantafyllidis, 2016a,b). KFS has an average grain size of $d_{50} = 0.14$ mm, a coefficient of uniformity of $C_u = d_{60}/d_{10} = 1.5$, a minimum void ratio of $e_{min} = 0.677$, and a maximum void ratio of $e_{max} = 1.054$. It is a quartz sand with a grain density of $\rho_s = 2.65$ g/cm^3 and a subangular particle shape. Additionally, some monotonic undrained hollow cylinder tests on Fraser River sand (FRS) from Uthayakumar and Vaid (1998) are also compared with the model predictions of HP+GIS+ACST. FRS has a median particle size of $d_{50} = 0.3$ mm, a coefficient of uniformity of $C_u = 2.4$, a minimum void ratio of $e_{min} = 0.68$, a maximum void ratio of $e_{max} = 1.0$, a grain density of $\rho_s = 2.72$ g/cm^3, and subangular to subrounded particles.

Besides the experimental data and the back-simulations using the novel HP+GIS+ACST, selected simulations are also presented using the HP+GIS in the version of Mugele et al. (2024b) and the HP+IS+ACST in the version of Liao and Yang (2021). For that purpose, all constitutive models are implemented in an Abaqus umat.for subroutine. The element test simulations are conducted using the program IncrementalDriver. IncrementalDriver and the umat.for for HP+GIS are freely available at the soilmodel.com website. For further details on the constitutive models, the reader is referred to the corresponding papers.

The used parameter sets for all constitutive models for KFS are listed in Table 1. The parameters of HP+GIS are taken from Mugele et al. (2024b) and the parameters of HP+IS+ACST are taken from Liao and Yang (2021). The parameters for the novel HP+GIS+ACST can be initially estimated using values from the aforementioned models. Since the effects of GIS and ACST overlap, some parameters have been adjusted. The calibration of the eight HP parameters is discussed in detail by Herle and Gudehus (1999), the calibration of the original five IS parameters is discussed in Niemunis and Herle (1997), and the calibration of the additional five GIS parameters considering cyclic preloading effects is shown in Duque et al. (2020). Guidance on the calibration of the five ACST parameters is provided by Liao and Yang (2021) and c_r is discussed in Barrero et al. (2020). Table 1 also provides HP+GIS and HP+GIS+ACST parameters for FRS, which have been generated based on a modification of the HP+IS+ACST parameters for FRS from Liao and Yang (2021). The parameter sets indicate that slight adjustments of the HP+GIS parameters may be necessary upon activation of the ACST due to the interaction between the individual model components.

Table 1 further indicates that some parts of the HP+GIS+ACST have been deactivated for both KFS and FRS, due to the unavailability of corresponding test data or the lack of investigation of these effects for the particular material. The anisotropy of the strength is deactivated for KFS by setting $\lambda = 0$ and the influence of the cyclic preloading Ω is deactivated for FRS by setting $\chi_0 = \chi_{max} = 1$. In this way, the HP+GIS+ACST can be significantly simplified or reduced to focus on the essential effects relevant to the problem under investigation. The importance of selecting a problem-related constitutive model is discussed by Carter (2024).

In the subsequent element test simulations using HP+GIS+ACST, the initial stress state $\boldsymbol{\sigma}_0$ and the void ratio e_0 are initialized according to the experiments. The relative density stated in the following figures is defined as $I_{D0} = (e_{max} - e)/(e_{max} - e_{min})$. The samples are assumed to undergo an isotropic compression before shearing, which would suggest a fully mobilized intergranular strain. However, even a very small disturbance (e.g. a slight vibration of the experimental setup) would quickly reduce this fully mobilized intergranular strain. Furthermore, a fully mobilized intergranular strain is unsuitable for the simulation of an effective stress path almost perpendicular to the p axis at the beginning of undrained tests. Therefore, the intergranular strain is assumed to be only partly mobilized in isotropic direction with $\boldsymbol{h}_0 = -0.77\ R/\sqrt{3}\ \boldsymbol{\delta}$ for KFS respectively $\boldsymbol{h}_0 = -0.5\ R/\sqrt{3}\ \boldsymbol{\delta}$ for FRS.

The initial fabric is assumed to be $F_0 = 0.5$ for the dry air pluviation technique used for the KFS and the water pluviation used for FRS, which is consistent with the initialization used in the literature (Gao et al., 2014; Gao and Zhao, 2015; Petalas et al., 2020; Yang et al., 2020; Liao and Yang, 2021). The further state variables are initialized to zero ($\Omega_0 = 0$, $H_0 = 0$). The initialized state variables in the simulations using HP+GIS and HP+IS+ACST are chosen accordingly.

Table 1
Parameter sets for the constitutive models HP+GIS, HP+IS+ACST and HP+GIS+ACST for Karlsruhe fine sand (KFS) and HP+GIS and HP+GIS+ACST for Fraser River sand (FRS).

		KFS			FRS	
		HP+GIS	HP+IS+ACST	HP+GIS+ACST	HP+GIS	HP+GIS+ACST
HP parameter	φ_c	33.1°			35°	
	h_s	4000 MPa			3000 MPa	
	n	0.27			0.33	
	e_{i0}	1.212			1.2	
	e_{c0}	1.054			1.029	
	e_{d0}	0.677			0.69	
	α	0.14		0.17	0.14	0.4
	β	2.5			1.2	
GIS/IS parameter	R	0.0001			0.00015	0.0003
	m_R	2.2			2.2	
	m_T	1.1			1.1	
	β_R	0.1	0.25	0.2	0.25	
	χ_R	5.5			2	
GIS parameter	γ_χ	2		2	4	
	χ_0	1.27		1.27	1††	
	χ_{max}	1.92		3.22	1††	
	C_Ω	48		60	0††	
	γ_Ω	1		1	1††	
ACST parameter	k_1		0.05	0.05		0.14
	k_2		0.4	0.4		0.6
	μ_0		180	25		500
	λ		0†	0†		0.38
	m		10	15		17
	α_D			0.3		0
	c_r			1†††		1†††

† anisotropic strength deactivated for KFS
†† cyclic preloading deactivated for FRS
††† decrease of the dilation history not calibrated

6.1. Anisotropy due to sedimentation

The mechanical behavior of sand can be significantly influenced by the angle α between the sedimentation axis and the direction of maximum principal stress, as defined in Fig. 7 for a conventional triaxial test under axisymmetric stress conditions. When the maximum principal stress is aligned with the sedimentation axis ($\alpha = 0°$), experiments show that sand exhibits greater stiffness and strength, as the major principal stress direction aligns with the preferred orientation of contact normals and is perpendicular to the bedding plane. In contrast, when the major principal stress is orthogonal to the sedimentation axis (parallel to the bedding plane) with $\alpha = 90°$, the samples behave more weakly, showing lower stiffness and increased contractancy (Arthur and Menzies, 1972; Oda, 1972; Ochiai and Lade, 1983; Yoshimine et al., 1998). This anisotropy effect is less pronounced in samples with higher particle sphericity.

Experimental data for KFS show that the influence of α on test results is small and practically negligible, which is mainly due to the less elongated grain shape (Wichtmann, 2016). However, to demonstrate the effect of α, triaxial undrained compression and extension tests with $p_0 = 200$ kPa, $e_0 = 0.9$ and $F_0 = 0.5$ under varying values of α have been simulated using the novel HP+GIS+ACST. Fig. 8 demonstrates, based on the deviatoric stress $q = \sigma_r - \sigma_a$ and the mean effective pressure p as a function of the axial strain ε_a, that the HP+GIS+ACST model reproduces the influence of α on the mechanical behavior of sand in triaxial compression as well as triaxial extension, although the effects for KFS are small. For larger values of α, the sample behaves softer and more contractive. The anisotropy can be increased by an increased value of the parameter k_1. The influence of α vanishes for an isotropic initial fabric $F_0 = 0$.

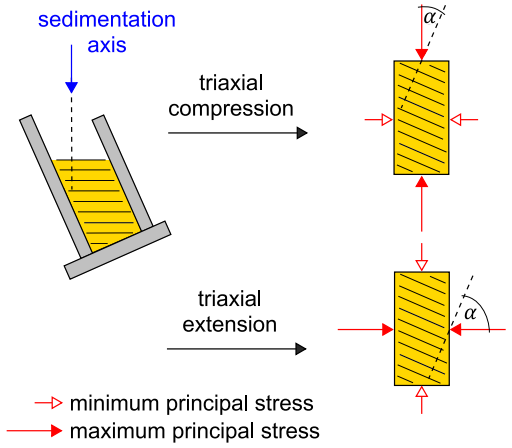

Fig. 7. Definition of the angle α between the sedimentation axis and the direction of maximum principal stress in a conventional triaxial compression or extension test with an axisymmetric stress state.

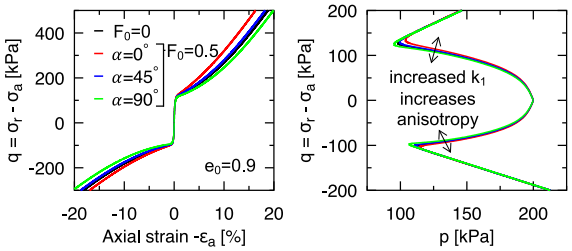

Fig. 8. Influence of the angle α on a monotonic undrained triaxial test on Karlsruhe fine sand ($e_0 = 0.9$) in simulations using HP+GIS+ACST: as α increases, the sample behaves softer and more contractive, although the effects for KFS are small (small parameter k_1).

A much stronger influence of the angle α has been documented by Uthayakumar and Vaid (1998) using undrained torsional shear tests (hollow cylinder test) on FRS. Fig. 9 shows the deviatoric stress $q = \sigma_3 - \sigma_1$ as a function of the mean effective pressure p and the shear strain $\gamma = \varepsilon_3 - \varepsilon_1$ for tests with $p_0 = 200$ kPa, $I_{D0} = 0.3$, and a constant value of the parameter $b = (\sigma_2 - \sigma_3)/(\sigma_1 - \sigma_3) = 0$ for different angles α. Note that σ_1, σ_3, ε_1, and ε_3 denote principal components of stress and strain. The pronounced anisotropic behavior of the sample can be seen and the response changes from dilative to contractive behavior with an increasing value of α. The recalculations with the HP+GIS+ACST, which are also shown in Fig. 9, can reproduce the experimental results quite well and thus adequately captures the pronounced anisotropic soil behavior. Additional simulations using HP+GIS in Fig. 9 demonstrate that the influence of α cannot be reproduced in a constitutive model without a fabric tensor.

6.2. Monotonic undrained triaxial tests

Monotonic undrained triaxial tests on KFS with $p_0 = 200$ kPa and different densities are considered in Fig. 10 for a triaxial compression and in Fig. 11 for a triaxial extension. The deviatoric stress $q = \sigma_r - \sigma_a$ as a function of the mean effective pressure p and the axial strain ε_a is shown. The experimental data from Wichtmann and Triantafyllidis (2016b) indicate a pronounced dependency of the material response on the density of the sample. Loose samples behave softer and more contractive than dense samples. Furthermore, the samples generally behave more contractive and softer during triaxial extension than during triaxial compression.

All six monotonic tests have been recalculated using the proposed HP+GIS+ACST model. The results show that the general density-dependent behavior of the material is qualitatively well reproduced, although some quantitative deviations between the test data and the simulations are observed. Nevertheless, the model effectively captures the stiffer and less contractive behavior of dense samples compared to loose samples. The differences between triaxial compression and extension are also modeled qualitatively and the samples behave more contractive due to triaxial extension. This difference can be mainly attributed to the ACST included in the model in combination with the initialization of the fabric tensor according to Eq. (29). At the beginning of a triaxial compression, $A > 1$ and at the beginning of a triaxial expansion, $A < 1$ applies for the FAV A, causing the behavior more contractive in the latter case.

6.3. Monotonic drained triaxial tests

Figs. 12 and 13 present the results for drained triaxial tests on initially loose and initially dense samples on KFS with $p_0 = 200$ kPa. Besides the monotonic drained triaxial tests from Wichtmann and Triantafyllidis (2016b), an additional test for each density was conducted in which five small unloading steps interrupt the monotonic deformation. The unloading of $\Delta q = 20$ kPa was performed after -2%, -4%, -6%, -8% and -10% axial strain. Figs. 12 and 13 contains the deviatoric stress $q = \sigma_r - \sigma_a$ as well as the volumetric strain $\varepsilon_v = \mathrm{tr}\,\boldsymbol{\varepsilon}$ as a function of the axial strain ε_a.

The loose sample does not show any peak strength and tends towards the asymptotic deviatoric stress, combined with a slight contractive volumetric behavior. The dense sample, on the other hand, first reaches a peak deviatoric stress before it also tends towards a similar asymptotic value. The dense sample reveals a pronounced volumetric expansion (dilatancy) and shows a significantly greater stiffness than the loose sample. The two experiments with the five small un- and reloading stages behave almost identically. The slight differences can be attributed to the different initial densities. In any case, the small unloading stages do not noticeably affect the overall behavior of the sample.

The recalculations with the three constitutive models HP+GIS, HP+IS+ACST, and HP+GIS+ACST provide comparable results for the purely monotonic test. It should be emphasized that all models underestimate the dilatancy of the dense sample and that the peak value of the deviatoric stress occurs at a smaller axial strain than in the experiments. These observations can be attributed to the deficits of the basic HP model, which have been addressed, for example, in neohyplasticity (Niemunis et al., 2016; Niemunis and Grandas Tavera, 2019; Mugele et al., 2024a).

In the recalculation of the tests with small unloading stages, a significant influence of the un- and reloadings can be seen in the HP+IS+ACST simulations. Immediately at the beginning of the reloading, the deviatoric stress reaches a significantly higher value than the value that would result from the purely monotonic path. This unrealistic response of the constitutive model, which corresponds to a dramatic overestimation of the shear strength, is known as overshooting and is a well-known problem of many advanced constitutive models (Duque et al., 2022; Tafili et al., 2024b). In addition to the effect on the stress–strain path, overshooting also impacts the volumetric response of the material. It is worth pointing out that overshooting is also to be expected in the original HP+IS model.

However, the GIS concept resolves the overshooting of the ASBS and the simulations using HP+GIS and HP+GIS+ACST do not show the issues mentioned above. The small un- and reloading stages result in curves very similar to the purely monotonic path.

For the simulations using the HP+GIS+ACST for the dense sample, Fig. 14 shows the FAV A, the individual fabric components F_{ij}, the norm of the fabric $\|\boldsymbol{F}\| = F$ and the scalar factor k as a function of the axial strain ε_a. A slight peak value of the fabric with $A > 1$ occurs due to

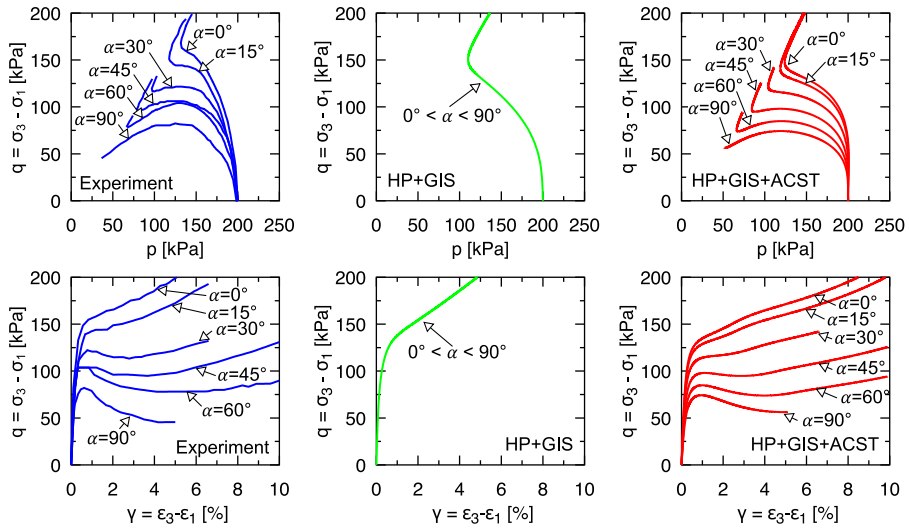

Fig. 9. Comparison between experimental data and model predictions (HP+GIS and HP+GIS+ACST) for undrained torsional shear tests with $b = 0$ on Fraser River sand for varying α ($p_0 = 200$ kPa, $I_{D0} = 0.3$) (experimental data from Uthayakumar and Vaid (1998)).

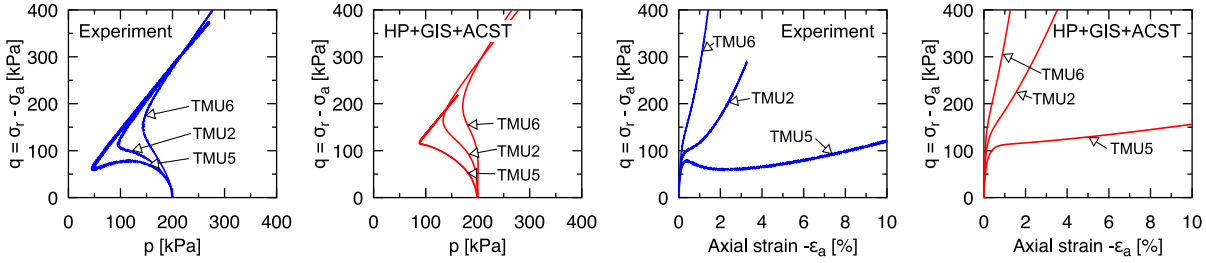

Fig. 10. Comparison between experimental data and model predictions (HP+GIS+ACST) for undrained triaxial compression tests on Karlsruhe fine sand (TMU2: $p_0 = 200$ kPa, $I_{D0} = 0.64$; TMU5: $p_0 = 200$ kPa, $I_{D0} = 0.29$; TMU6: $p_0 = 200$ kPa, $I_{D0} = 0.87$) (experimental data from Wichtmann and Triantafyllidis (2016b)).

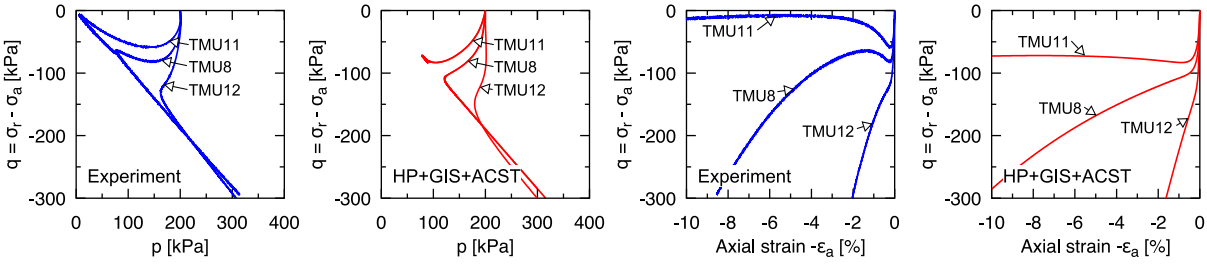

Fig. 11. Comparison between experimental data and model predictions (HP+GIS+ACST) for undrained triaxial extension tests on Karlsruhe fine sand (TMU8: $p_0 = 200$ kPa, $I_{D0} = 0.53$; TMU11: $p_0 = 200$ kPa, $I_{D0} = 0.24$; TMU12: $p_0 = 200$ kPa, $I_{D0} = 0.94$) (experimental data from Wichtmann and Triantafyllidis (2016b)).

the dense sample. Due to the theoretical aspects discussed in Section 5 and mainly to avoid the artificial hardening issue, the parameter set is chosen so that the peak in A is not particularly pronounced. The critical state with $A^{\text{asy,c}} = \|\boldsymbol{F}^{\text{asy,c}}\| = F^{\text{asy,c}} = 1$ is asymptotically reached. Due to the applied axisymmetric deformation and the corresponding initialization of the fabric, $F_a = -2\,F_r$ applies throughout the entire deformation. Immediately after a load direction reversal, the FAV A jumps from A_1 to $A_2 = -A_1$. The individual components of the fabric show a continuous curve without jumps. Likewise, the scalar factor k exhibits jumps due to a change in loading direction, although the associated state variable of the intergranular strain $\boldsymbol{h}$ evolves continuously (not shown).

6.4. Cyclic undrained triaxial tests with strain cycles

The results of cyclic undrained triaxial tests with a prescribed strain amplitude of $\varepsilon_a^{\text{ampl}} = 10^{-2}$ is shown for a loose sample in Fig. 15, for a medium-dense sample in Fig. 16 and for a dense sample in Fig. 17. All tests conducted using KFS by Wichtmann and Triantafyllidis (2016a) start at an isotropic initial stress state with $p_0 = 200$ kPa. The figures present the deviatoric stress $q = \sigma_r - \sigma_a$ as a function of the mean effective pressure p and the axial strain ε_a.

Due to the applied cyclic loading, soil liquefaction ($p = 0$) is reached after several cycles in the experiments irrespective of the density. The initial density significantly affects the number of cycles required before reaching liquefaction: the denser the sample, the more cycles can be applied and the corresponding pore pressure build-up is slower. The maximum deviatoric stress is reached at the end of the first loading phase and increases with increasing density. With an increasing number of cycles, the mean effective pressure decreases, resulting in a substantial reduction in stiffness. Finally, if the soil gets liquefied ($p = 0$), the observed shear stiffness vanishes.

The recalculations of the test on loose sand using the three constitutive models show good agreement with the experimental results, as

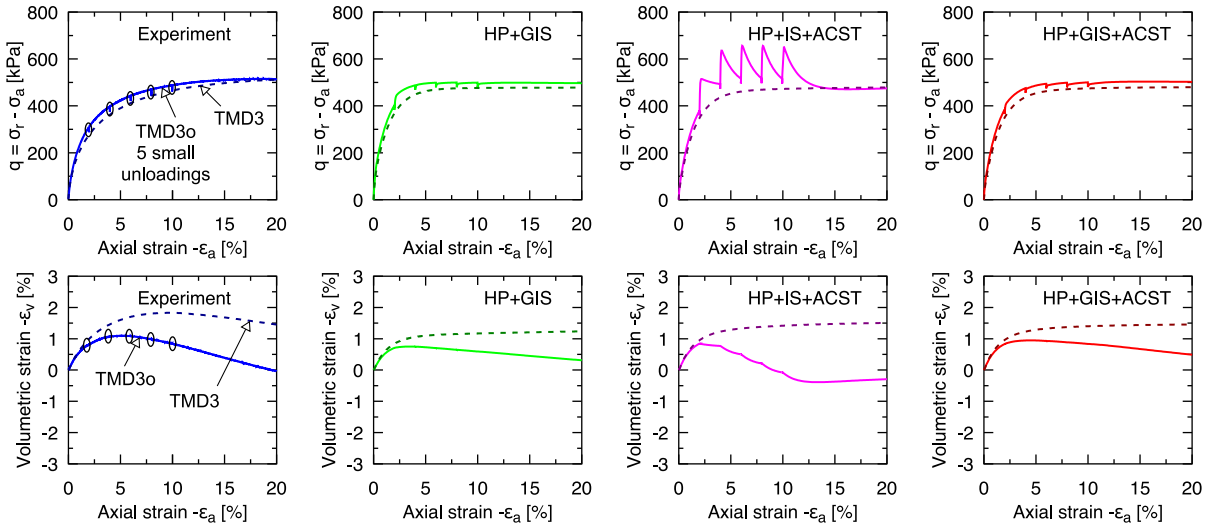

Fig. 12. Comparison between experimental data and models prediction (HP+GIS, HP+IS+ACST, and HP+GIS+ACST) for drained triaxial tests on Karlsruhe fine sand (TMD3: $p_0 = 200$ kPa, $I_{D0} = 0.21$ and TMD3o: $p_0 = 200$ kPa, $I_{D0} = 0.33$) (purely monotonic test TMD3 from Wichtmann and Triantafyllidis (2016b)).

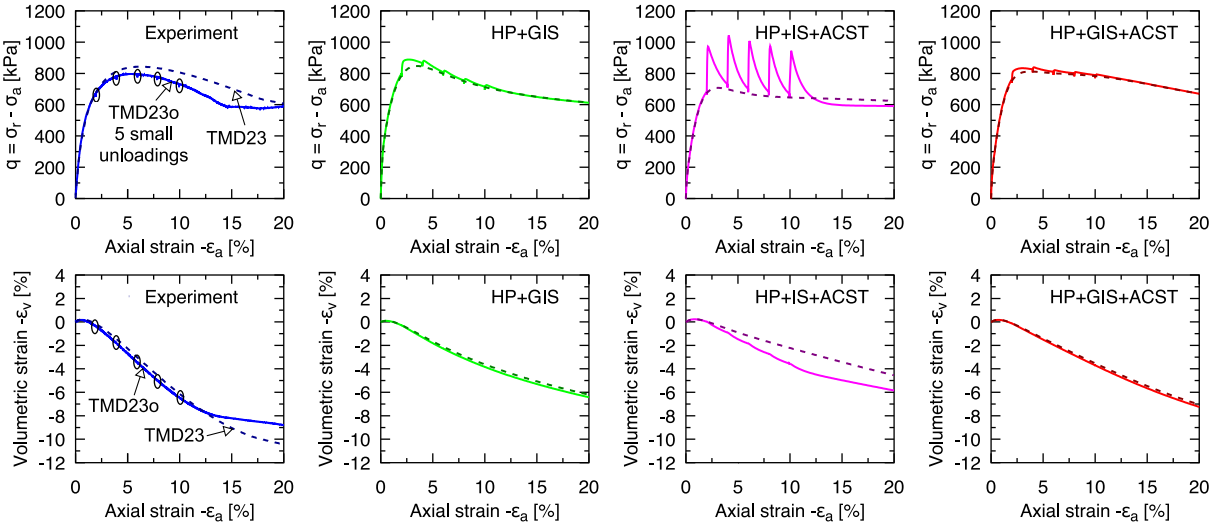

Fig. 13. Comparison between experimental data and models prediction (HP+GIS, HP+IS+ACST, and HP+GIS+ACST) for drained triaxial tests on Karlsruhe fine sand (TMD23: $p_0 = 200$ kPa, $I_{D0} = 0.92$ and TMD23o: $p_0 = 200$ kPa, $I_{D0} = 0.93$) (purely monotonic test TMD23 from Wichtmann and Triantafyllidis (2016b)).

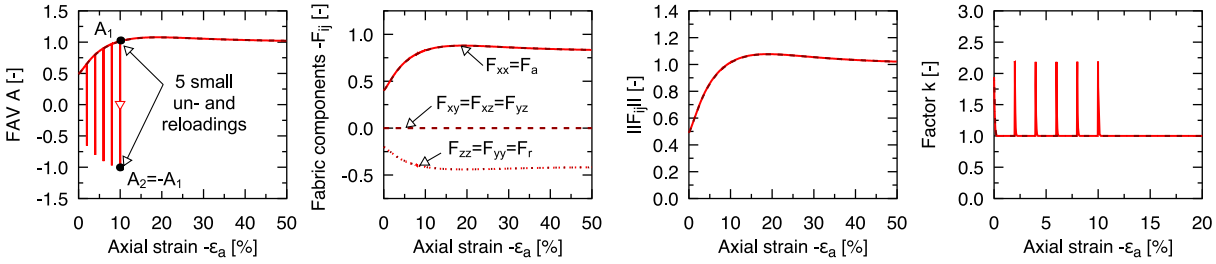

Fig. 14. Evolution of the FAV A, of the components of the fabric tensor F_{ij}, the norm of the fabric tensor $\|\boldsymbol{F}\|$ and the scalar factor k in the simulations of the tests TMD23 and TMD23o using HP+GIS+ACST.

shown in Fig. 15. If the sample becomes denser, the simulations with HP+GIS do not capture the soil liquefaction. The difference between the HP+GIS simulations and the experimental results is most pronounced for the densest sample, as shown in Fig. 17. Because the soil liquefaction is not reached, the shear stiffness does not vanish even after a large number of cycles, which leads to an unrealistic stress–strain curve. It is worth mentioning that the described deficit of the HP+GIS should also be expected in the original HP+IS model as shown for example by Duque et al. (2022).

In contrast, the simulations using HP+IS+ACST and HP+GIS+ACST show realistic results and soil liquefaction even in dense sand after several cycles corresponding to the respective experiment. The simulated

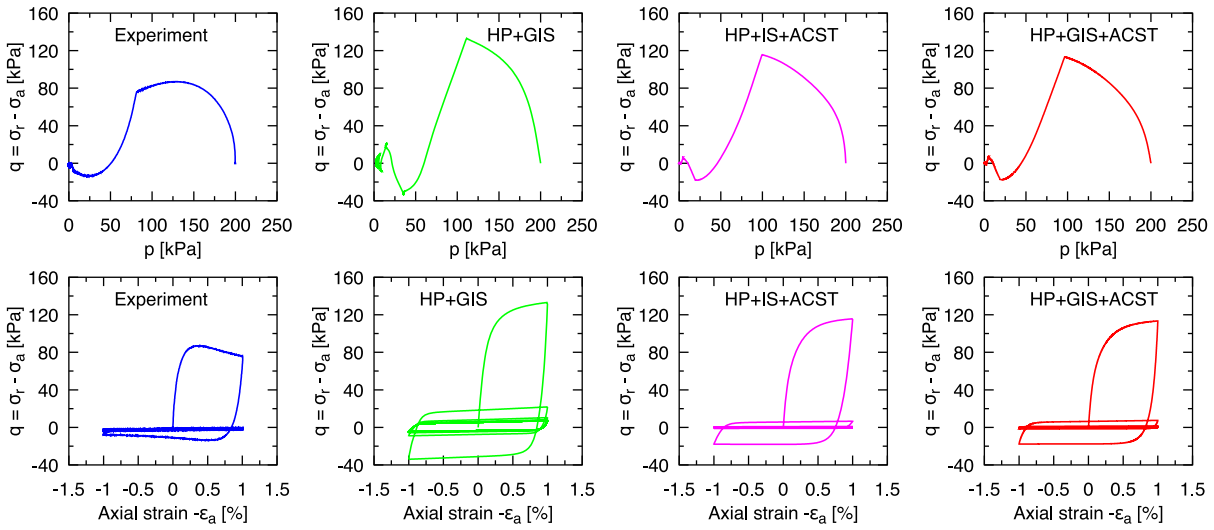

Fig. 15. Comparison between experimental data and models prediction (HP+GIS, HP+IS+ACST, and HP+GIS+ACST) for an undrained cyclic triaxial test with strain cycles on Karlsruhe fine sand (TCUE15: $p_0 = 200$ kPa, $\varepsilon_a^{\text{ampl}} = 10^{-2}$, $I_{D0} = 0.29$) (experimental data from Wichtmann and Triantafyllidis (2016a)).

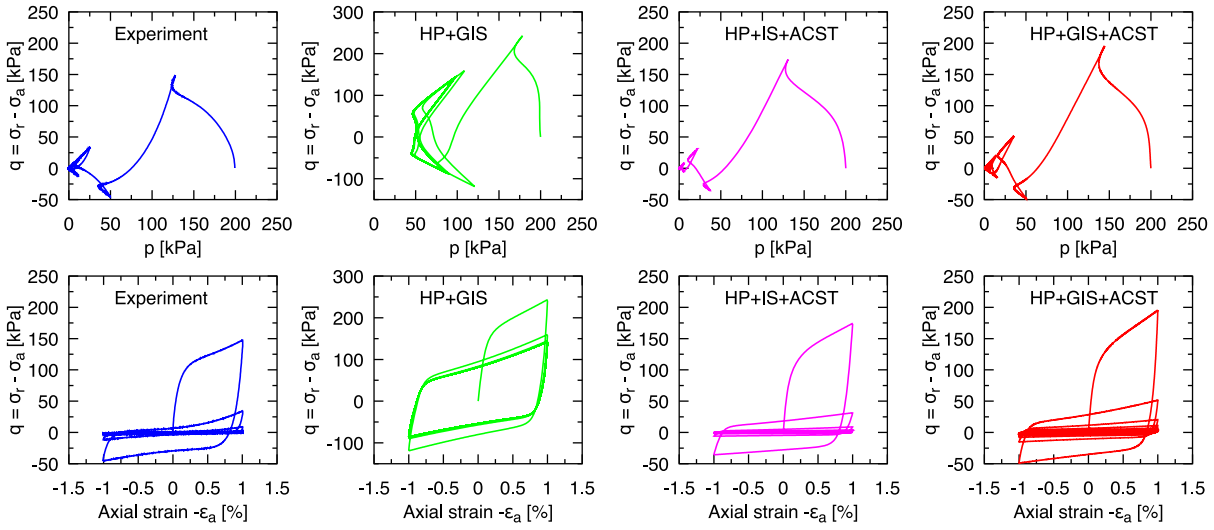

Fig. 16. Comparison between experimental data and models prediction (HP+GIS, HP+IS+ACST, and HP+GIS+ACST) for an undrained cyclic triaxial test with strain cycles on Karlsruhe fine sand (TCUE16: $p_0 = 200$ kPa, $\varepsilon_a^{\text{ampl}} = 10^{-2}$, $I_{D0} = 0.66$) (experimental data from Wichtmann and Triantafyllidis (2016a)).

stress–strain curves are also comparable with the experimental results. The incorporation of the ACST into HP+GIS has significantly improved the simulation results of cyclic tests involving the simulation of cyclic soil liquefaction. This is consistent with the general observation that constitutive models accounting for an evolving fabric are better at reproducing cyclic soil liquefaction effects (Dafalias and Manzari, 2004; Fuentes et al., 2020; Liao et al., 2022; Tafili et al., 2024a).

Fig. 18 shows for the simulations for the dense sample using HP+GIS+ACST from Fig. 17 the FAV A and the individual components of the anisotropic fabric F_{ij} as a function of the number of cycles N, the dilation history H as a function of the mobilized friction angle φ_{mob}, as well as the state mobilization S, the scalar factor k, and the cyclic preloading Ω as a function of the axial strain ε_a. The cyclic loading with a given strain amplitude causes a reduction of the initialized anisotropic fabric with an increasing number of cycles. A smaller strain amplitude would lead asymptotically to $A \to 0$ and $F \to 0$, which is known as a shakedown. With each reversal of loading direction, the FAV A jumps from A_1 to $A_2 = -A_1$. The evolution of the fabric-related quantities corresponds qualitatively to the results of current discrete element simulations from the literature by Mo et al. (2024). Since the dense soil exhibits dilative behavior in some phases of the simulation at large values of the mobilized friction angle, an accumulative increase of the dilatancy history H occurs. Fig. 18 also shows that the state of the soil at the beginning and during the first cycles lies inside the ASBS ($S < 0$). With an increasing number of cycles (reduced effective pressure with the same void ratio), the state reaches the ASBS ($S \approx 1$) before each change in the loading direction. Immediately after a load direction reversal, the scalar factor k exhibits its maximum value of $k = m_R$. With increasing deformation after the reversal, however, the factor reduces to $k \to 1$. The relatively large strain amplitude causes no significant build-up of the cyclic preloading variable Ω. The latter would become relevant for cyclic deformations with smaller strain amplitudes.

A cyclic undrained triaxial test on a dense sample with a smaller strain amplitude of $\varepsilon_a^{\text{ampl}} = 6 \cdot 10^{-4}$ than in the tests considered previously is presented in Fig. 19. A large number of cycles is required in the experiment to reach liquefaction. While the HP+GIS can successfully represent this increased number of cycles, the HP+IS+ACST exhibits a significantly faster onset of cyclic liquefaction compared to the experiment. The contractancy after a reversal in the loading direction is overestimated in these simulations. Combined with this overestimated decrease in mean effective pressure, the shear stiffness

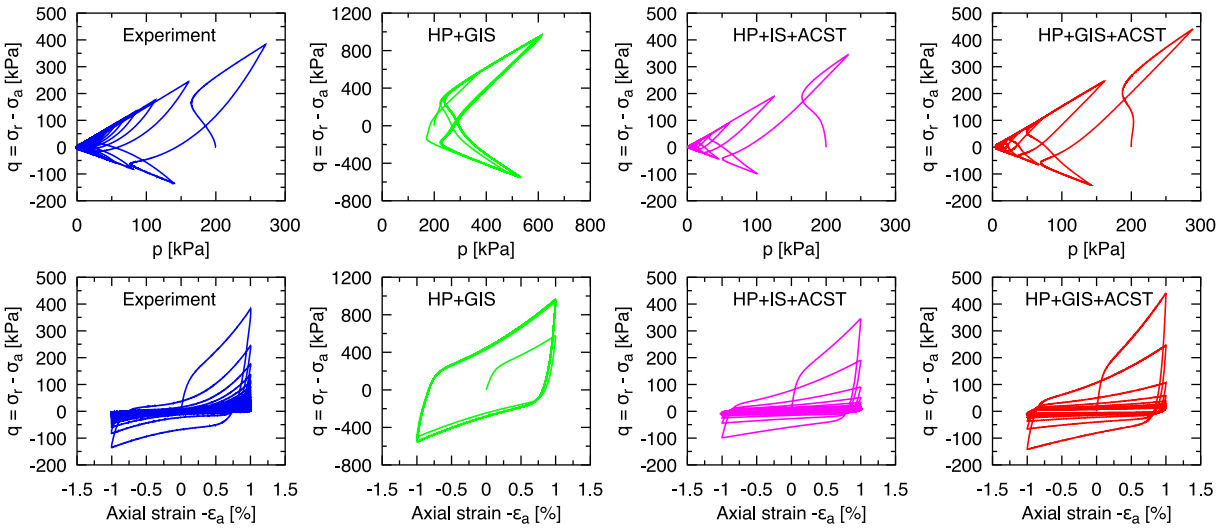

Fig. 17. Comparison between experimental data and models prediction (HP+GIS, HP+IS+ACST, and HP+GIS+ACST) for an undrained cyclic triaxial test with strain cycles on Karlsruhe fine sand (TCUE17: $p_0 = 200$ kPa, $\varepsilon_a^{\text{ampl}} = 10^{-2}$, $I_{D0} = 0.94$) (experimental data from Wichtmann and Triantafyllidis (2016a)).

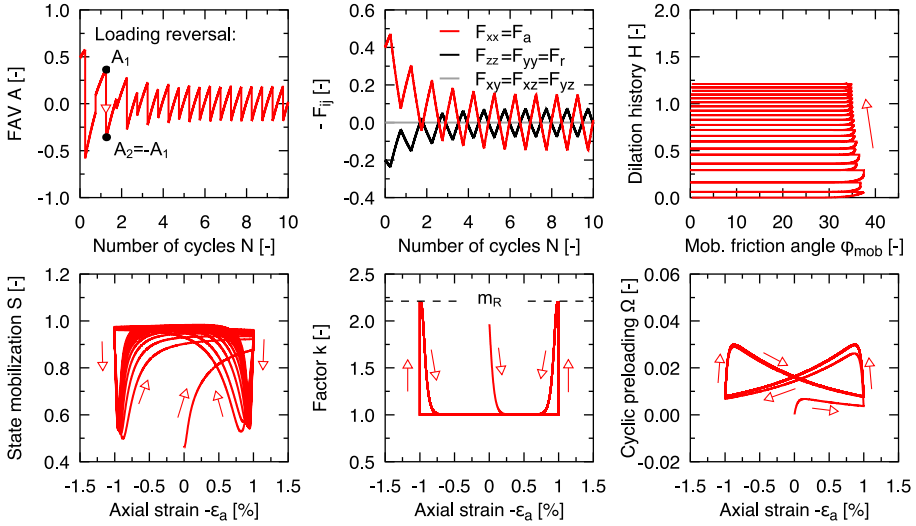

Fig. 18. Evolution of the FAV A and the components of the fabric tensor F_{ij} as a function of the number of cycles N, the dilation history H as a function of the mobilized friction angle φ_{mob} and the state mobilization S, the scalar factor k and the cyclic preloading Ω as a function of the axial strain ε_a in the simulations of the test TCUE17 using HP+GIS+ACST.

also reduced significantly during the first cycles. The excessive accumulation observed in this case is linked to the coupling with the ACST. Although HP+GIS+ACST shows slower accumulation compared to HP+IS+ACST, the accumulation simulated with HP+GIS+ACST is still too fast compared to the experiment.

6.5. Cyclic undrained triaxial tests with stress cycles

Fig. 20 presents a cyclic undrained triaxial test on a sample of KFS with a specified deviatoric stress amplitude of $q^{\text{ampl}} = 40$ kPa and an isotropic initial stress state with $p_0 = 200$ kPa. Again, the deviatoric stress q is shown as a function of the mean effective pressure p and as a function of the axial strain ε_a. The tests show a rather fast decrease in the mean effective pressure within the first few cycles. After the first cycles, the rate of accumulation is considerably reduced. The accumulation accelerates again when the mean effective pressure is significantly decreased. Finally, the sample undergoes the so-called cyclic mobility, in which the stress path shows the typical butterfly shape including momentary liquefaction ($p \approx 0$) while the strain amplitude increases cycle by cycle. However, even in this state, axial strain occurs in both compression and extension within each cycle, although a strain accumulation is observed in the extension direction. Cyclic mobility was reached after 145 cycles in the experiment.

Neither the HP+GIS nor the HP+IS+ACST can reproduce this behavior accurately. While the HP+GIS captures the non-linear accumulation effects and the number of cycles required to reach cyclic mobility, it fails to simulate the butterfly-shaped stress path or the momentary state $p \approx 0$. Additionally, a pronounced one-way ratcheting of the axial strain occurs in this simulation stage. The HP+IS+ACST can reproduce the cyclic mobility but it fails to simulate the non-linear accumulation producing an excessively fast reduction in the mean effective pressure. The strain amplitude during cyclic mobility is also too large compared to the experiment.

The HP+GIS+ACST combines the benefits of both HP+GIS and HP+IS+ACST and can therefore qualitatively and quantitatively reproduce the non-linear accumulation effects, the number of cycles to reach cyclic mobility, and the cyclic mobility itself. In addition, the increasing strain amplitude with the number of cycles and its accumulation in the extension direction in cyclic mobility are also accurately captured by the HP+GIS+ACST.

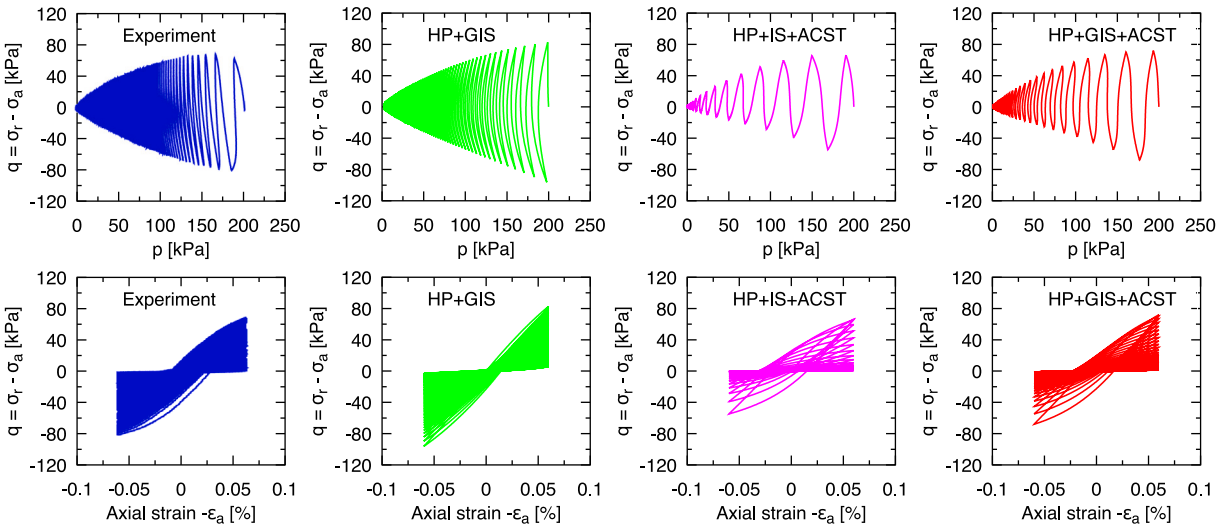

Fig. 19. Comparison between experimental data and models prediction (HP+GIS, HP+IS+ACST, and HP+GIS+ACST) for an undrained cyclic triaxial test with strain cycles on Karlsruhe fine sand (TCUE9: $p_0 = 200$ kPa, $\varepsilon_a^{\text{ampl}} = 6 \cdot 10^{-4}$, $I_D = 0.67$) (experimental data from Wichtmann and Triantafyllidis (2016a)).

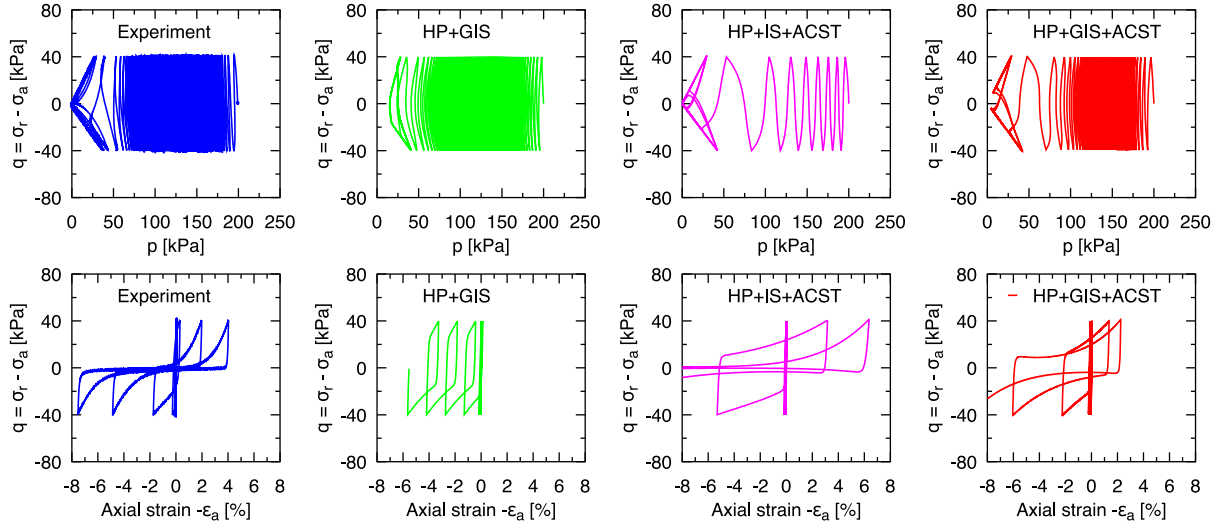

Fig. 20. Comparison between experimental data and models prediction (HP+GIS, HP+IS+ACST, and HP+GIS+ACST) for an undrained cyclic triaxial test with stress cycles on Karlsruhe fine sand (TCUI11: $p_0 = 200$ kPa, $q^{\text{ampl}} = 40$ kPa, $I_D = 0.56$) (experimental data from Wichtmann and Triantafyllidis (2016a)).

7. Conclusion

A new hypoplastic constitutive model called HP+GIS+ACST is presented, which is suitable to simulate cyclic deformations and also considers the influence of the anisotropic fabric on the mechanical behavior of soil. This is demonstrated using element test simulations and a comparison with experimental data as well as simulations of two other hypoplastic models. The comparison with experimental data, performed on Karlsruhe fine sand (KFS) and Fraser River sand (FRS), includes both monotonic and cyclic tests, and shows that the presented model performs well. The proposed HP+GIS+ACST outperforms previous hypoplastic models from the literature

The HP+GIS+ACST is derived by coupling the generalized intergranular strain (GIS) (Mugele et al., 2024b) concept with the anisotropic critical state theory (ACST) (Li and Dafalias, 2012). Some important theoretical aspects that generally should be considered by coupling a constitutive model with the ACST have been emphasized. The novel model includes six state variables ($\boldsymbol{\sigma}$, e, $\boldsymbol{h}$, Ω, $\boldsymbol{F}$, H) and requires 25 parameters. Parts of the HP+GIS+ACST can be easily deactivated, making it adaptable to specific problem requirements.

The HP+GIS+ACST resolves well-known problems of earlier formulations such as overshooting of the ASBS and not completely reaching the cyclic liquefaction in dense samples. Nevertheless, the evolution equation of the anisotropic fabric is still insufficient for all possible loading scenarios and should be improved in the future.

CRediT authorship contribution statement

L. Mugele: Writing – original draft, Validation, Methodology, Formal analysis, Visualization, Software, Investigation, Conceptualization. **H.H. Stutz:** Supervision, Project administration, Funding acquisition, Writing – review & editing, Resources, Methodology, Conceptualization. **Z.X. Yang:** Writing – review & editing, Supervision, Project administration, Funding acquisition, Validation, Resources, Methodology.

Declaration of competing interest

The authors declare that they have no known competing financial interests or personal relationships that could have appeared to influence the work reported in this paper.

Acknowledgments

The authors are grateful for the financial support provided by the Sino-German Center for Research Promotion under the Mobility project (Grant No. M-0489). The authors would like to thank Dr. D. Liao for the fruitful discussions during this research.

Appendix A. Notation and abbreviations

The mechanical sign convention is used throughout this paper. Extension strain and tensile stress are therefore positive. Second-order tensors are written in bold letters (e.g., $\boldsymbol{\sigma}$ or $\boldsymbol{N}$), with $\|\sqcup\|$ denoting the Euclidean norm and $\mathrm{tr}\,\sqcup$ representing the sum of diagonal components of the corresponding tensor $\sqcup$. Normalized tensors are denoted as $\vec{\sqcup} = \sqcup/\|\sqcup\|$. The deviatoric part of a second-order tensor $\sqcup$ is denoted with $\sqcup^*$. Fourth-order tensors are symbolized using capital sans-serif letters (e.g., L). The symbol $\cdot$ denotes multiplication with one dummy index (single contraction), for instance, the scalar product of two first-order tensors can be written as $\boldsymbol{a}\cdot\boldsymbol{b}$. The multiplication with two dummy indices (double contraction) is written using a colon, for example, $\boldsymbol{a}:\boldsymbol{b}$. Dyadic multiplication is written as $\boldsymbol{ab}$. The unit tensor of second-order ($\boldsymbol{\delta}$) and fourth-order tensor (I) are defined. Stresses are effective in the sense of Therzaghi. The following abbreviations are used:

ACST	Anisotropic critical state theory (Li and Dafalias, 2012)
ASBS	Asymptotic state boundary surface
CSL	Critical state line
DSL	Dilatancy state line
FAV	Fabric anisotropy variable
GIS	Generalized intergranular strain (Mugele et al., 2024b)
HP	Hypoplasticity after von Wolffersdorff (1996)
IS	Intergranular strain after Niemunis and Herle (1997)
KFS	Karlsruhe fine sand
FRS	Fraser River sand

Appendix B. HP formulation after von Wolffersdorff (1996)

This appendix summarizes the equations of the hypoplasticity after von Wolffersdorff (1996) (HP). The constitutive model assumes the relation between the stress rate and the strain rate

$$\dot{\boldsymbol{\sigma}} = f_s \mathsf{L} : \dot{\boldsymbol{\epsilon}} + f_s f_d \boldsymbol{N}\|\dot{\boldsymbol{\epsilon}}\| \tag{B.1}$$

with

$$\mathsf{L} = \frac{1}{\hat{\boldsymbol{\sigma}}:\hat{\boldsymbol{\sigma}}}\left(\left(F^{\mathrm{hyp}}\right)^2 \mathsf{I} + a^2\hat{\boldsymbol{\sigma}}\hat{\boldsymbol{\sigma}}\right) \tag{B.2}$$

and

$$\boldsymbol{N} = \frac{F^{\mathrm{hyp}}\, a}{\hat{\boldsymbol{\sigma}}:\hat{\boldsymbol{\sigma}}}(\hat{\boldsymbol{\sigma}} + \hat{\boldsymbol{\sigma}}^*)\,, \tag{B.3}$$

where $I_{ijkl} = 0.5(\delta_{ik}\delta_{jl} + \delta_{il}\delta_{jk})$ is a fourth-order unity tensor and $\boldsymbol{\delta}$ is a second-order unity tensor with

$$\hat{\boldsymbol{\sigma}} = \frac{\boldsymbol{\sigma}}{\mathrm{tr}\,\boldsymbol{\sigma}} \qquad \text{and} \qquad \hat{\boldsymbol{\sigma}}^* = \hat{\boldsymbol{\sigma}} - \frac{1}{3}\boldsymbol{\delta} \tag{B.4}$$

with

$$a = \sqrt{\frac{3}{8}}\frac{(3-\sin\varphi_c)}{\sin\varphi_c} \tag{B.5}$$

and

$$F_0^{\mathrm{hyp}} = \sqrt{\frac{1}{8}\tan^2\psi + \frac{2-\tan^2\psi}{2+\sqrt{2}\tan\psi\cos(3\theta)}} - \frac{1}{2\sqrt{2}}\tan\psi \tag{B.6}$$

with

$$\tan\psi = \sqrt{3}\|\hat{\boldsymbol{\sigma}}^*\| \tag{B.7}$$

and

$$\cos(3\theta) = -\sqrt{6}\frac{\mathrm{tr}(\hat{\boldsymbol{\sigma}}^*\cdot\hat{\boldsymbol{\sigma}}^*\cdot\hat{\boldsymbol{\sigma}}^*)}{[\hat{\boldsymbol{\sigma}}^*:\hat{\boldsymbol{\sigma}}^*]^{3/2}}\,. \tag{B.8}$$

The scalar factors f_s (barotropy factor) and f_d (pyknotropy factor) take into account the influence of mean effective pressure and density:

$$f_s = \frac{h_s}{n}\left(\frac{e_i}{e}\right)^{\beta}\frac{1+e_i}{e_i}\left(\frac{-\mathrm{tr}\,\boldsymbol{\sigma}}{h_s}\right)^{1-n}\left[3 + a^2 - a\sqrt{3}\left(\frac{e_{i0}-e_{d0}}{e_{c0}-e_{d0}}\right)^{\alpha}\right]^{-1}, \tag{B.9}$$

$$f_d = \left(\frac{e-e_d}{e_c-e_d}\right)^{\alpha}\,. \tag{B.10}$$

The characteristic void ratios (e_i, e_c and e_d) decrease with increasing mean pressure:

$$\frac{e_i}{e_{i0}} = \frac{e_d}{e_{d0}} = \frac{e_c}{e_{c0}} = \exp\left[-\left(\frac{3p}{h_s}\right)^n\right]\,. \tag{B.11}$$

The HP model requires 8 parameters:

$\varphi_c, h_s, n, e_{d0}, e_{c0}, e_{i0}, \alpha$ and β.

Data availability

Data will be made available on reasonable request including an implementation of the HP+GIS+ACST model in terms of an umat.for subroutine for Abaqus or an udsm.dll for Plaxis.

References

Adesina, P., O'Sullivan, C., Wang, T., 2023. DEM study on the effect of particle shape on the shear behaviour of granular materials. Comput. Part. Mech. (ISSN: 2196-4386) 1–20. http://dx.doi.org/10.1007/s40571-023-00632-8.

Andrianopoulos, K.I., Papadimitriou, A.G., Bouckovalas, G.D., 2010. Bounding surface plasticity model for the seismic liquefaction analysis of geostructures. Soil Dyn. Earthq. Eng. (ISSN: 02677261) 30 (10), 895–911. http://dx.doi.org/10.1016/j.soildyn.2010.04.001.

Arthur, J.R.F., Menzies, B.K., 1972. Inherent anisotropy in sand. Géotechnique (ISSN: 0016-8505) 22 (1), 115–128.

Barrero, A.R., Taiebat, M., Dafalias, Y.F., 2020. Modeling cyclic shearing of sands in the semifluidized state. Int. J. Numer. Anal. Methods Geomech. (ISSN: 0363-9061) 44 (3), 371–388. http://dx.doi.org/10.1002/nag.3007.

Bauer, E., 1996. Calibration of a comprehensive hypoplastic model for granular materials. Soils Found. (ISSN: 00380806) 36 (1), 13–26. http://dx.doi.org/10.3208/sandf.36.13.

Been, K., Jefferies, M.G., 1985. A state parameter for sands. Géotechnique (ISSN: 0016-8505) 35 (2), 99–112. http://dx.doi.org/10.1680/geot.1985.35.2.99.

Bode, M., Fellin, W., Mašín, D., Medicus, G., Ostermann, A., 2020. An intergranular strain concept for material models formulated as rate equations. Int. J. Numer. Anal. Methods Geomech. (ISSN: 03639061) 44 (7), 1003–1018. http://dx.doi.org/10.1002/nag.3043.

Boulanger, R., Ziotopoulou, K., 2022. PM4sand (version 3.2): A sand plasticity model for earthquake engineering applications. URL https://pm4sand.engr.ucdavis.edu/.

Carter, J.P., 2024. Constitutive modelling in computational geomechanics – 61st rankine lecture, British geotechnical association, 2023. Géotechnique (ISSN: 0016-8505) 74 (13), 1511–1535. http://dx.doi.org/10.1680/jgeot.23.RL.001.

Chrisopoulos, S., Vogelsang, J., 2019. A finite element benchmark study based on experimental modeling of vibratory pile driving in saturated sand. Soil Dyn. Earthq. Eng. (ISSN: 02677261) 122, 248–260. http://dx.doi.org/10.1016/j.soildyn.2019.01.001.

Dafalias, Y.F., Manzari, M.T., 2004. Simple plasticity sand model accounting for fabric change effects. J. Eng. Mech. (ISSN: 0733-9399) 130 (6), 622–634. http://dx.doi.org/10.1061/(ASCE)0733-9399(2004)130:6(622).

Duque, J., Mašín, D., Fuentes, W., 2020. Improvement to the intergranular strain model for larger numbers of repetitive cycles. Acta Geotech. (ISSN: 1861-1125) 15 (12), 3593–3604. http://dx.doi.org/10.1007/s11440-020-01073-w.

Duque, J., Yang, M., Fuentes, W., Mašín, D., Taiebat, M., 2022. Characteristic limitations of advanced plasticity and hypoplasticity models for cyclic loading of sands. Acta Geotech. (ISSN: 1861-1125) 17 (6), 2235–2257. http://dx.doi.org/10.1007/s11440-021-01418-z.

Fuentes, W., Triantafyllidis, T., 2015. ISA model: A constitutive model for soils with yield surface in the intergranular strain space. Int. J. Numer. Anal. Methods Geomech. (ISSN: 03639061) 39 (11), 1235–1254. http://dx.doi.org/10.1002/nag.2370.

Fuentes, W., Wichtmann, T., Gil, M., Lascarro, C., 2020. ISA-hypoplasticity accounting for cyclic mobility effects for liquefaction analysis. Acta Geotech. (ISSN: 1861-1125) 15 (6), 1513–1531. http://dx.doi.org/10.1007/s11440-019-00846-2.

Gao, Z., Zhao, J., 2015. Constitutive modeling of anisotropic sand behavior in monotonic and cyclic loading. J. Eng. Mech. (ISSN: 0733-9399) 141 (8), http://dx.doi.org/10.1061/(ASCE)EM.1943-7889.0000907.

Gao, Z., Zhao, J., Li, X.-S., Dafalias, Y.F., 2014. A critical state sand plasticity model accounting for fabric evolution. Int. J. Numer. Anal. Methods Geomech. (ISSN: 03639061) 38 (4), 370–390. http://dx.doi.org/10.1002/nag.2211.

Gudehus, G., 1996. A comprehensive constitutive equation for granular materials. Soils Found. (ISSN: 00380806) 36 (1), 1–12. http://dx.doi.org/10.3208/sandf.36.1.

Gudehus, G., 2011. Physical Soil Mechanics. Springer Berlin Heidelberg.

Gudehus, G., Mašín, D., 2009. Graphical representation of constitutive equations. Géotechnique (ISSN: 0016-8505) 59 (2), 147–151. http://dx.doi.org/10.1680/geot.2007.00155.

Guo, N., Zhao, J., 2013. The signature of shear-induced anisotropy in granular media. Comput. Geotech. (ISSN: 0266352X) 47, 1–15. http://dx.doi.org/10.1016/j.compgeo.2012.07.002.

Herle, I., Gudehus, G., 1999. Determination of parameters of a hypoplastic constitutive model from properties of grain assemblies. Mech. Cohes.-Frict. Mater. (ISSN: 1082-5010) 4 (5), 461–486. http://dx.doi.org/10.1002/(SICI)1099-1484(199909)4:5461::AID-CFM713.0.CO;2-P.

Kirkgard, M.M., Lade, P.V., 1993. Anisotropic three-dimensional behavior of a normally consolidated clay. Can. Geotech. J. (ISSN: 0008-3674) 30 (5), 848–858. http://dx.doi.org/10.1139/t93-075.

Kolymbas, D., 1988. Eine Konstitutive Theorie für Böden und Andere Körnige Stoffe (Ph.D. thesis). Universität Fridericiana in Karlsruhe, Institut für Bodenmechanik und Felsmechnik, Issue 109, Karlsruhe.

Kolymbas, D., 1991a. Computer-aided design of constitutive laws. Int. J. Numer. Anal. Methods Geomech. (ISSN: 0363-9061) 15 (8), 593–604. http://dx.doi.org/10.1002/nag.1610150806.

Kolymbas, D., 1991b. An outline of hypoplasticity. Arch. Appl. Mech. (ISSN: 0939-1533) 61 (3), 143–151. http://dx.doi.org/10.1007/BF00788048.

Li, X.S., Dafalias, Y.F., 2012. Anisotropic critical state theory: Role of fabric. J. Eng. Mech. (ISSN: 0733-9399) 138 (3), 263–275. http://dx.doi.org/10.1061/(ASCE)EM.1943-7889.0000324.

Li, X., Li, X.-S., 2009. Micro-macro quantification of the internal structure of granular materials. J. Eng. Mech. (ISSN: 0733-9399) 135 (7), 641–656. http://dx.doi.org/10.1061/(ASCE)0733-9399(2009)135:7(641).

Liao, D., Yang, Z.X., 2021. Hypoplastic modeling of anisotropic sand behavior accounting for fabric evolution under monotonic and cyclic loading. Acta Geotech. (ISSN: 1861-1125) 16 (7), 2003–2029. http://dx.doi.org/10.1007/s11440-020-01127-z.

Liao, D., Yang, Z., Wang, S., Wu, W., 2022. Hypoplastic model with fabric change effect and semifluidized state for post–liquefaction cyclic behavior of sand. Int. J. Numer. Anal. Methods Geomech. (ISSN: 0363-9061) 46 (17), 3154–3177. http://dx.doi.org/10.1002/nag.3444.

Mašín, D., 2012. Hypoplastic Cam–Clay model. Géotechnique (ISSN: 0016-8505) 62 (6), 549–553. http://dx.doi.org/10.1680/geot.11.T.019.

Mašín, D., 2013. Clay hypoplasticity with explicitly defined asymptotic states. Acta Geotech. (ISSN: 1861-1125) 8 (5), 481–496. http://dx.doi.org/10.1007/s11440-012-0199-y.

Mašín, D., 2019. Modelling of Soil Behaviour with Hypoplasticity. Springer International Publishing, Cham, ISBN: 978-3-030-03975-2, http://dx.doi.org/10.1007/978-3-030-03976-9.

Mašín, D., Herle, I., 2005. State boundary surface of a hypoplastic model for clays. Comput. Geotech. (ISSN: 0266352X) 32 (6), 400–410. http://dx.doi.org/10.1016/j.compgeo.2005.09.001.

Mašín, D., Herle, I., 2006. State boundary surface in hypoplasticity. In: Wu, W., Yu, H.-S. (Eds.), Moderne Trends in Geomechanics. In: Springer Proceedings in Physics, Springer, Berlin, ISBN: 9783540251354, pp. 117–128. http://dx.doi.org/10.1007/978-3-540-35724-77.

Matsuoka, H., Nakai, T., 1977. Stress-strain relationship of soil based on the SMP, constitutive equations of soils. In: Murayama, S., Schofield, A.N. (Eds.), Speciality Session 9.

Miura, S., Toki, S., 1982. A sample preparation method and its effect on static and cyclic deformation-strength properties of sand. Soils Found. (ISSN: 00380806) 22 (1), 61–77. http://dx.doi.org/10.3208/sandf1972.22.61.

Miura, S., Toki, S., 1984. Anisotropy in mechanical properties and its simulation of sands sampled from natural deposits. Soils Found. (ISSN: 00380806) 24 (3), 69–84.

Mo, W., Wang, R., Zhang, J.-M., Dafalias, Y.F., 2024. Quantification of fabric evolution in granular material under cyclic loading. Int. J. Numer. Anal. Methods Geomech. (ISSN: 0363-9061) 48 (3), 701–726. http://dx.doi.org/10.1002/nag.3658.

Mugele, L., Niemunis, A., Stutz, H.H., 2024a. Neohypoplasticity revisited. Int. J. Numer. Anal. Methods Geomech. (ISSN: 0363-9061) 48 (1), 311–331. http://dx.doi.org/10.1002/nag.3640.

Mugele, L., Stutz, H.H., Mašín, D., 2024b. Generalized intergranular strain concept and its application to hypoplastic models. Comput. Geotech. (ISSN: 0266352X) (173), 106480. http://dx.doi.org/10.1016/j.compgeo.2024.106480.

Nemat-Nasser, S., Tobita, Y., 1982. Influence of fabric on liquefaction and densification potential of cohesionless sand. Mech. Mater. (ISSN: 0167-6636) 1 (1), 43–62. http://dx.doi.org/10.1016/0167-6636(82)90023-0.

Niemunis, A., 2003. Extended Hypoplastic Models for Soils (Habilitation). Ruhr-Universität Bochum, Bochum.

Niemunis, A., Grandas Tavera, C.E., 2019. Essential concepts of neohypoplasticity. In: Wu, Wei (Ed.), Desiderata Geotechnica. In: Springer eBooks Engineering, Springer, Cham, ISBN: 9783030149871, pp. 132–142. http://dx.doi.org/10.1007/978-3-030-14987-116.

Niemunis, A., Grandas Taverna, C.E., Wichtmann, T., 2016. Peak stress obliquity in drained and undrained sands. Simulations with neohypoplasticity. In: Triantafyllidis, T. (Ed.), Holistic Simulation of Geotechnical Installation Processes: Benchmarks and Simulations. Springer International Publishing, pp. 85–114. http://dx.doi.org/10.1007/978-3-319-23159-45.

Niemunis, A., Herle, I., 1997. Hypoplastic model for cohesionless soils with elastic strain range. Mech. Cohes.-Frict. Mater. (ISSN: 1082-5010) 2 (4), 279–299. http://dx.doi.org/10.1002/(SICI)1099-1484(199710)2:4279::AID-CFM293.0.CO;2-8.

Niemunis, A., Nübel, K., Karcher, C., 2000. The consistency conditions for density limits of hypoplastic constitutive law. Task Q. (4), 412–420.

Norlyk, P., Sørensen, K., Andersen, L.V., Sørensen, K.K., Stutz, H.H., 2020. Holistic simulation of a subsurface inflatable geotechnical energy storage system using fluid cavity elements. Comput. Geotech. (ISSN: 0266352X) 127, 103722. http://dx.doi.org/10.1016/j.compgeo.2020.103722.

Ochiai, H., Lade, P.V., 1983. Three-dimensional behavior of sand with anisotropic fabric. J. Geotech. Eng. ASCE 109 (10), 1313–1328.

Oda, M., 1972. Initial fabrics and their relations to mechanical properties of granular material. Soils Found. (ISSN: 00380806) 12 (1), 17–36.

Petalas, A.L., Dafalias, Y.F., Papadimitriou, A.G., 2019. SANISAND–FN: An evolving fabric–based sand model accounting for stress principal axes rotation. Int. J. Numer. Anal. Methods Geomech. (ISSN: 0363-9061) 43 (1), 97–123. http://dx.doi.org/10.1002/nag.2855.

Petalas, A.L., Dafalias, Y.F., Papadimitriou, A.G., 2020. SANISAND-F: Sand constitutive model with evolving fabric anisotropy. Int. J. Solids Struct. (ISSN: 0020-7683) 188–189, 12–31. http://dx.doi.org/10.1016/j.ijsolstr.2019.09.005.

Poblete, M., Fuentes, W., Triantafyllidis, T., 2016. On the simulation of multidimensional cyclic loading with intergranular strain. Acta Geotech. (ISSN: 1861-1125) 11 (6), 1263–1285. http://dx.doi.org/10.1007/s11440-016-0492-2.

Roscoe, K.H., Schofield, A.N., Wroth, C.P., 1958. On the yielding of soils. Géotechnique (ISSN: 0016-8505) 8 (1), 22–53.

Schofield, A.N., Wroth, C.P., 1968. Critical state soil mechanics.

Staubach, P., Machaček, J., Wichtmann, T., 2021. Large-deformation analysis of pile installation with subsequent lateral loading: Sanisand vs. Hypoplasticity. Soil Dyn. Earthq. Eng. (ISSN: 0267-7261) 151, 106964. http://dx.doi.org/10.1016/j.soildyn.2021.106964.

Tafili, M., Duque, J., Mašín, D., Wichtmann, T., 2024a. A hypoplastic model for pre- and post-liquefaction analysis of sands. Comput. Geotech. (ISSN: 0266352X) 171, 106314. http://dx.doi.org/10.1016/j.compgeo.2024.106314.

Tafili, M., Duque, J., Mašín, D., Wichtmann, T., 2024b. Repercussion of overshooting effects on elemental and finite-element simulations. Int. J. Geomech. (ISSN: 1532-3641) 24 (3), http://dx.doi.org/10.1061/IJGNAI.GMENG-8842.

Uthayakumar, M., Vaid, Y.P., 1998. Static liquefaction of sands under multiaxial loading. Can. Geotech. J. (ISSN: 0008-3674) 35 (2), 273–283. http://dx.doi.org/10.1139/t98-007.

von Wolffersdorff, P.-A., 1996. A hypoplastic relation for granular materials with a predefined limit state surface. Mech. Cohesive- Frict. Mater. (ISSN: 1082-5010) 1 (3), 251–271. http://dx.doi.org/10.1002/(SICI)1099-1484(199607)1:3251::AID-CFM133.0.CO;2-3.

Wang, R., Cao, W., Xue, L., Zhang, J.-M., 2021. An anisotropic plasticity model incorporating fabric evolution for monotonic and cyclic behavior of sand. Acta Geotech. (ISSN: 1861-1133) 16 (1), 43–65. http://dx.doi.org/10.1007/s11440-020-00984-y.

Wang, R., Dafalias, Y.F., Fu, P., Zhang, J.-M., 2020. Fabric evolution and dilatancy within anisotropic critical state theory guided and validated by DEM. Int. J. Solids Struct. (ISSN: 0020-7683) 188–189, 210–222. http://dx.doi.org/10.1016/j.ijsolstr.2019.10.013.

Wang, R., Pinzón, G., Andò, E., Viggiani, G., 2022. Modeling combined fabric evolution in an anisometric granular material driven by particle-scale X-ray measurements. J. Eng. Mech. (ISSN: 1943-7889) 148 (1), 04021120. http://dx.doi.org/10.1061/(ASCE)EM.1943-7889.0002032.

Wegener, D., Herle, I., 2014. Prediction of permanent soil deformations due to cyclic shearing with a hypoplastic constitutive model. Geotechnik (ISSN: 0172-6145) 37 (2), 113–122. http://dx.doi.org/10.1002/gete.201300013.

Wichtmann, T., 2016. Soil Behaviour Under Cyclic Loading - Experimental Observations, Constitutive Description and Applications (Habilitation). Karlsruhe Institute of Technology , Institute of Soil Mechanics and Rock Mechanics (IBF), Issue 181, Karlsruhe.

Wichtmann, T., Triantafyllidis, T., 2016a. An experimental database for the development, calibration and verification of constitutive models for sand with focus to cyclic loading: part II—tests with strain cycles and combined loading. Acta Geotech. (ISSN: 1861-1125) 11 (4), 763–774. http://dx.doi.org/10.1007/s11440-015-0412-x.

Wichtmann, T., Triantafyllidis, T., 2016b. An experimental database for the development, calibration and verification of constitutive models for sand with focus to cyclic loading: part I—tests with monotonic loading and stress cycles. Acta Geotech. (ISSN: 1861-1125) 11 (4), 739–761. http://dx.doi.org/10.1007/s11440-015-0402-z.

Wiebicke, M., Herle, I., Andò, E., Viggiani, G., 2021. Measuring the fabric evolution of sand – application and challenges. Geotechnik (ISSN: 0172-6145) 44 (2), 114–122. http://dx.doi.org/10.1002/gete.202000019.

Wu, W., 1992. Hypoplastizität als Mathematisches Modell Zum Mechanischen Verhalten Granularer Stoffe (Ph.D. thesis). Universität Fridericiana in Karlsruhe, Institut für Bodenmechanik und Felsmechnik, Issue 129, Karlsruhe.

Wu, W., Bauer, E., 1994. A simple hypoplastic constitutive model for sand. Int. J. Numer. Anal. Methods Geomech. (ISSN: 0363-9061) 18 (12), 833–862. http://dx.doi.org/10.1002/nag.1610181203.

Xie, Y.H., Yang, Z.X., Barreto, D., Jiang, M.D., 2017. The influence of particle geometry and the intermediate stress ratio on the shear behavior of granular materials. Granul. Matter (ISSN: 1434-7636) 19 (2), 1–13. http://dx.doi.org/10.1007/s10035-017-0723-8.

Yang, Z.X., Li, X.S., Yang, J., 2008. Quantifying and modelling fabric anisotropy of granular soils. Géotechnique (ISSN: 0016-8505) 58 (4), 237–248. http://dx.doi.org/10.1680/geot.2008.58.4.237.

Yang, Z., Liao, D., Xu, T., 2020. A hypoplastic model for granular soils incorporating anisotropic critical state theory. Int. J. Numer. Anal. Methods Geomech. (ISSN: 0363-9061) 44 (6), 723–748. http://dx.doi.org/10.1002/nag.3025.

Yang, Z.X., Wu, Y., 2017. Critical state for anisotropic granular materials: A discrete element perspective. Int. J. Geomech. (ISSN: 1532-3641) 17 (2), 04016054. http://dx.doi.org/10.1061/(ASCE)GM.1943-5622.0000720.

Yang, Z.X., Xu, T.T., Chen, Y.N., 2018. Unified modeling of the influence of consolidation conditions on monotonic soil response considering fabric evolution. J. Eng. Mech. (ISSN: 0733-9399) 144 (8), 04018073. http://dx.doi.org/10.1061/(ASCE)EM.1943-7889.0001499.

Yoshimine, M., Ishihara, K., Vargas, W., 1998. Effects of principal stress direction and intermediate principal stress on undrained shear behavior of sand. Soils Found. (ISSN: 00380806) 38 (3), 179–188. http://dx.doi.org/10.3208/sandf.38.3179.